

Imaging the Meissner effect in hydride superconductors using quantum sensors

<https://doi.org/10.1038/s41586-024-07026-7>

Received: 14 May 2023

Accepted: 3 January 2024

Published online: 28 February 2024

 Check for updates

P. Bhattacharyya^{1,2,16}, W. Chen^{3,16}, X. Huang^{3,16}, S. Chatterjee^{1,4}, B. Huang⁵, B. Kobrin^{1,2}, Y. Lyu¹, T. J. Smart^{1,6}, M. Block⁷, E. Wang⁸, Z. Wang⁷, W. Wu⁷, S. Hsieh^{1,2}, H. Ma⁵, S. Mandayam⁷, B. Chen⁷, E. Davis¹, Z. M. Geballe⁹, C. Zu¹⁰, V. Struzhkin¹¹, R. Jeanloz⁶, J. E. Moore^{1,2}, T. Cui^{3,12}, G. Galli^{5,13,14}, B. I. Halperin⁷, C. R. Laumann¹⁵ & N. Y. Yao^{1,2,7}✉

By directly altering microscopic interactions, pressure provides a powerful tuning knob for the exploration of condensed phases and geophysical phenomena¹. The megabar regime represents an interesting frontier, in which recent discoveries include high-temperature superconductors, as well as structural and valence phase transitions^{2–6}. However, at such high pressures, many conventional measurement techniques fail. Here we demonstrate the ability to perform local magnetometry inside a diamond anvil cell with sub-micron spatial resolution at megabar pressures. Our approach uses a shallow layer of nitrogen-vacancy colour centres implanted directly within the anvil^{7–9}; crucially, we choose a crystal cut compatible with the intrinsic symmetries of the nitrogen-vacancy centre to enable functionality at megabar pressures. We apply our technique to characterize a recently discovered hydride superconductor, CeH₉ (ref. 10). By performing simultaneous magnetometry and electrical transport measurements, we observe the dual signatures of superconductivity: diamagnetism characteristic of the Meissner effect and a sharp drop of the resistance to near zero. By locally mapping both the diamagnetic response and flux trapping, we directly image the geometry of superconducting regions, showing marked inhomogeneities at the micron scale. Our work brings quantum sensing to the megabar frontier and enables the closed-loop optimization of superhydride materials synthesis.

The recent proliferation of work on superhydride materials—hydrogen-rich compounds containing rare-earth or actinide elements—is part of a long-standing search for superconductivity at room temperature^{10–24}. The intuition underlying this approach dates back nearly half a century²⁵: the minimal mass of hydrogen and covalent bonding lead to the presence of both high-frequency phonons and strong electron–phonon interactions. The combination of these features is predicted to favour the formation of Cooper pairs, and thus superconductivity, at relatively high temperatures²⁶. This strategy has been fruitful, leading to the discovery and characterization of nearly a dozen superconducting hydrides in the past decade^{2,3}. The synthesis of these materials relies on the application of megabar (100 GPa) pressures using diamond anvil cells (DACs). This requirement naturally constrains the size and homogeneity of the samples, markedly complicating attempts at *in situ* characterization. For example, it is extremely challenging for conventional probes to image the geometry of superconducting grains or to measure local properties.

This challenge is particularly acute for studying the magnetic signatures of superconductivity^{27,28}. Typical probes of magnetism average over the entire DAC geometry thereby discarding information encoded in local spatial features. The ability to perform spatially resolved magnetometry near the hydride sample would overcome these challenges and enable both enhanced field sensitivities and local measurements of the Meissner effect and flux trapping. Doing so together with resistance measurements would allow us to simultaneously probe the key electrical and magnetic signatures of superconductivity.

In this work, we develop a platform for metrology at megabar pressures based on the nitrogen-vacancy (NV) colour centre in diamond^{7–9,29}. By instrumenting diamond anvils with shallow ensembles of NV centres, we directly image both the local diamagnetic response and flux trapping with sub-micron resolution in a cerium superhydride (CeH₉). Our main results are three-fold. First, by using NVs embedded in a [111]-crystal cut anvil (Fig. 1), we demonstrate the ability to perform both d.c. and a.c. magnetometry at pressures up to around 140 GPa. Second, leveraging

¹Department of Physics, University of California, Berkeley, CA, USA. ²Materials Science Division, Lawrence Berkeley National Laboratory, Berkeley, CA, USA. ³State Key Laboratory of Superhard Materials, College of Physics, Jilin University, Changchun, China. ⁴Department of Physics, Carnegie Mellon University, Pittsburgh, PA, USA. ⁵Department of Chemistry, University of Chicago, Chicago, IL, USA. ⁶Department of Earth and Planetary Science, University of California, Berkeley, CA, USA. ⁷Department of Physics, Harvard University, Cambridge, MA, USA. ⁸Department of Chemistry and Chemical Biology, Harvard University, Cambridge, MA, USA. ⁹Earth and Planets Laboratory, Carnegie Institution of Washington, Washington, DC, USA. ¹⁰Department of Physics, Washington University in St. Louis, St. Louis, MO, USA. ¹¹Center for High Pressure Science and Technology Advanced Research, Shanghai, China. ¹²School of Physical Science and Technology, Ningbo University, Ningbo, China. ¹³Materials Science Division and Center for Molecular Engineering, Argonne National Laboratory, Lemont, IL, USA. ¹⁴Pritzker School of Molecular Engineering, University of Chicago, Chicago, IL, USA. ¹⁵Department of Physics, Boston University, Boston, MA, USA. ¹⁶These authors contributed equally: P. Bhattacharyya, W. Chen, X. Huang. ✉e-mail: nyao@fas.harvard.edu

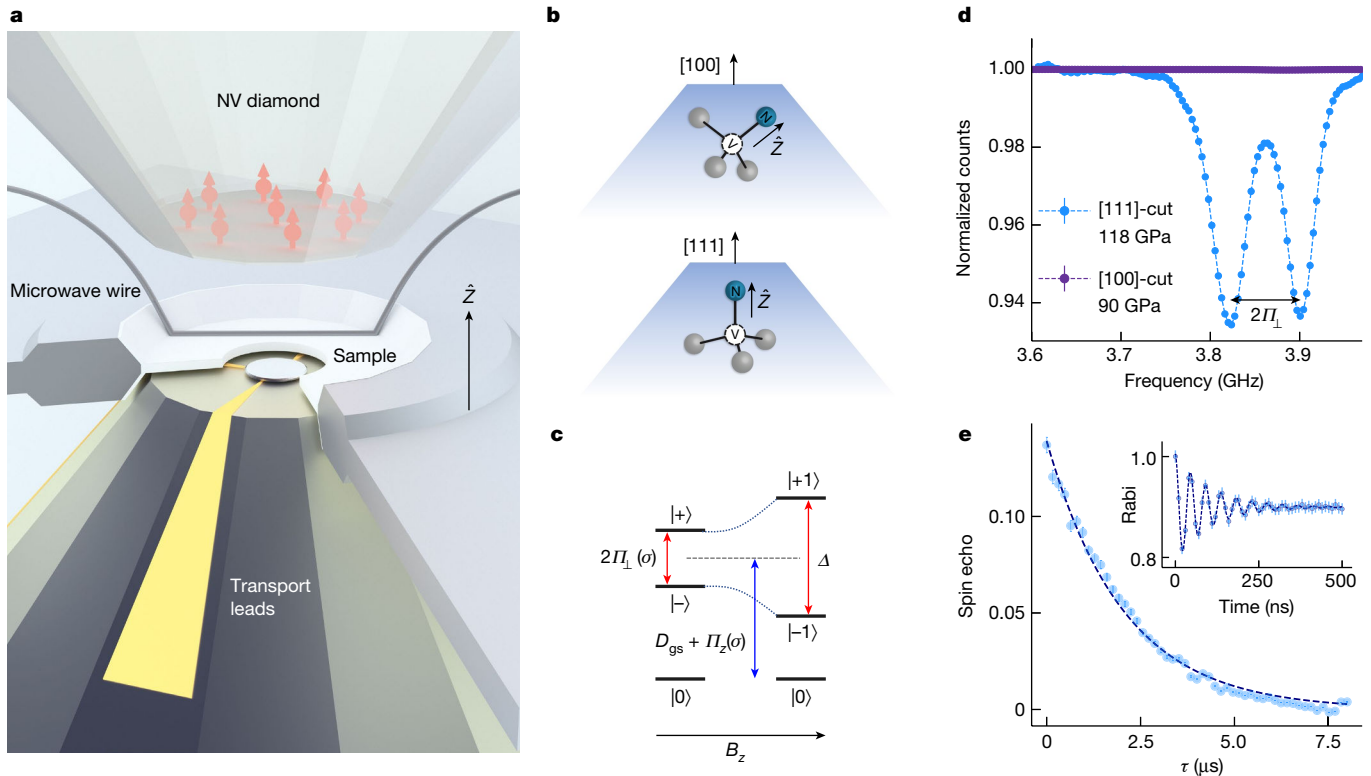


Fig. 1 | NV sensing at megabar pressures. **a**, Schematic of the sample loading showing CeH_9 compressed between two opposing anvils. The top anvil contains a shallow layer of NV centres (about 1 ppm density) approximately 50 nm below the culet surface. For ODMR measurements, a platinum wire is placed on the top culet to deliver microwaves. **b**, The quantization axis (\hat{z}) of the NV centre defines its local frame. The crystal cut of the diamond anvil determines the projection of culet stresses in the NV frame. For a [100]-cut anvil (top), the dominant culet stresses (σ_{zz} and σ_{\perp}) break the C_{3v} -symmetry of all four NV subgroups. For a [111]-cut anvil (bottom), these stresses preserve the C_{3v} -symmetry of the specific NV subgroup whose quantization axis is coincident with the loading axis (shown). For this particular NV subgroup, we observe excellent ODMR contrast up to a pressure of about 140 GPa. **c**, Schematic of the spin sublevels of

the NV in the presence of stress and magnetic field. Symmetry-preserving stresses, quantified by Π_z , directly add to the zero-field splitting, D_{gs} , whereas symmetry-breaking stresses induce a splitting, $2\Pi_{\perp}$. An axial magnetic field B_z induces a Zeeman splitting that adds in quadrature to the stress splitting. **d**, A continuous-wave ODMR measurement on a [111]-cut anvil (sample S1) showing about 6% contrast at around 118 GPa and a splitting, $2\Pi_{\perp} \approx (2\pi) \times 78$ MHz (blue data points). For comparison, the ODMR contrast in a [100]-cut anvil at about 90 GPa is approximately 0.01% (purple data points). **e**, A spin echo (that is, pulsed) measurement on sample S2 at 137 GPa yields an NV coherence time, $T_2^{\text{echo}} = 2.04(4)$ μs . We demonstrate Rabi frequencies of up to about $(2\pi) \times 25$ MHz (inset).

this ability, we show that CeH_9 locally suppresses an external magnetic field after zero-field cooling. On field cooling, we observe the partial expulsion of magnetic fields below the superconducting transition temperature, T_c , as determined by simultaneous electrical resistance measurements. By spatially mapping these observations, we are able to directly measure the size and geometry of the superconducting regions. Finally, by cycling both magnetic fields and temperature, we investigate the presence of hysteresis in the magnetization. We observe signatures of flux trapping, the strength of which depends on the temperature and cooling history.

Our experiments are performed on two independent samples (S1 and S2) of cerium superhydride prepared by laser heating inside miniature panoramic diamond anvil cells³⁰ (Fig. 2a–d) (Methods). Four-point electrical transport measurements (Fig. 2e–f) on both samples exhibit a sharp drop in resistance at $T_c \approx 90$ K, suggesting the formation of CeH_9 (ref. 10). For each DAC, the top anvil is a type Ib [111]-cut anvil, which is implanted with a layer of NV centres about 50 nm below the culet surface at a density of approximately 1 ppm (refs. 7,8). Each NV centre hosts a spin-1 electronic ground state governed by the Hamiltonian, $H_0 = D_{gs} S_z^2$. Here, S are the spin-1 operators of the NV with the N–V axis defining the quantization axis (\hat{z}) and $D_{gs} = (2\pi) \times 2.87$ GHz is the zero-field splitting between the $|m_s = 0\rangle$ spin sub-level and the degenerate $|m_s = \pm 1\rangle$ sub-levels³¹. Local perturbations such as temperature, stress, electric field and magnetic field couple to the NV

centre and change the energy of its spin states^{32–37}. These changes can be read out using optically detected magnetic resonance (ODMR) spectroscopy in which we measure a change in the fluorescence of the NV on chirping a microwave field through resonance³⁸ (Methods).

Our central explorations of CeH_9 involve local measurements (at ≥ 100 GPa) of the magnetic field at the NV centre, B_z , as we tune the temperature, T , and an external magnetic field, H_z , applied along the NV axis, \hat{z} . Thus, it is crucial to be able to separate the effects of crystal stress and temperature from the ODMR spectrum of the NV, to accurately measure B_z . This is a relatively straightforward task. At megabar pressures, the effects of stress dominate over those of temperature by nearly three orders of magnitude (Methods), so we focus on deconvolving the effects of the local stress tensor, σ . Stress couples to the NV centre by the effective Hamiltonian, $H_S = \Pi_z S_z^2 + \Pi_x (S_y^2 - S_x^2) + \Pi_y (S_x S_y + S_y S_x)$, where the parameters $\Pi_i = \Pi_i(\sigma)$ depend on the appropriate components of σ (Methods). Π_z captures the additional zero-field splitting due to C_{3v} -symmetry-preserving stresses^{7,37} (Fig. 1c). Meanwhile, $\Pi_{\perp} = \sqrt{\Pi_x^2 + \Pi_y^2}$ parametrizes the symmetry-breaking stresses, mixing the $|m_s = \pm 1\rangle$ spin states into new eigenstates, $|\pm\rangle = (|m_s = +1\rangle \pm e^{i\phi_{\Pi}} |m_s = -1\rangle)/\sqrt{2}$, which are split by $2\Pi_{\perp}$ (Fig. 1c,d); here, $\phi_{\Pi} = \arctan(\Pi_y/\Pi_x)$. As the Zeeman splitting from an axial magnetic field adds in quadrature with the stress splitting, the ODMR spectrum of the NV exhibits a pair of resonances with a total splitting of $\Delta = \sqrt{(2\Pi_{\perp})^2 + (2\gamma_B B_z)^2}$, where $\gamma_B = (2\pi) \times 2.8$ MHz G⁻¹ is the gyromagnetic ratio of the NV (Fig. 1c). This

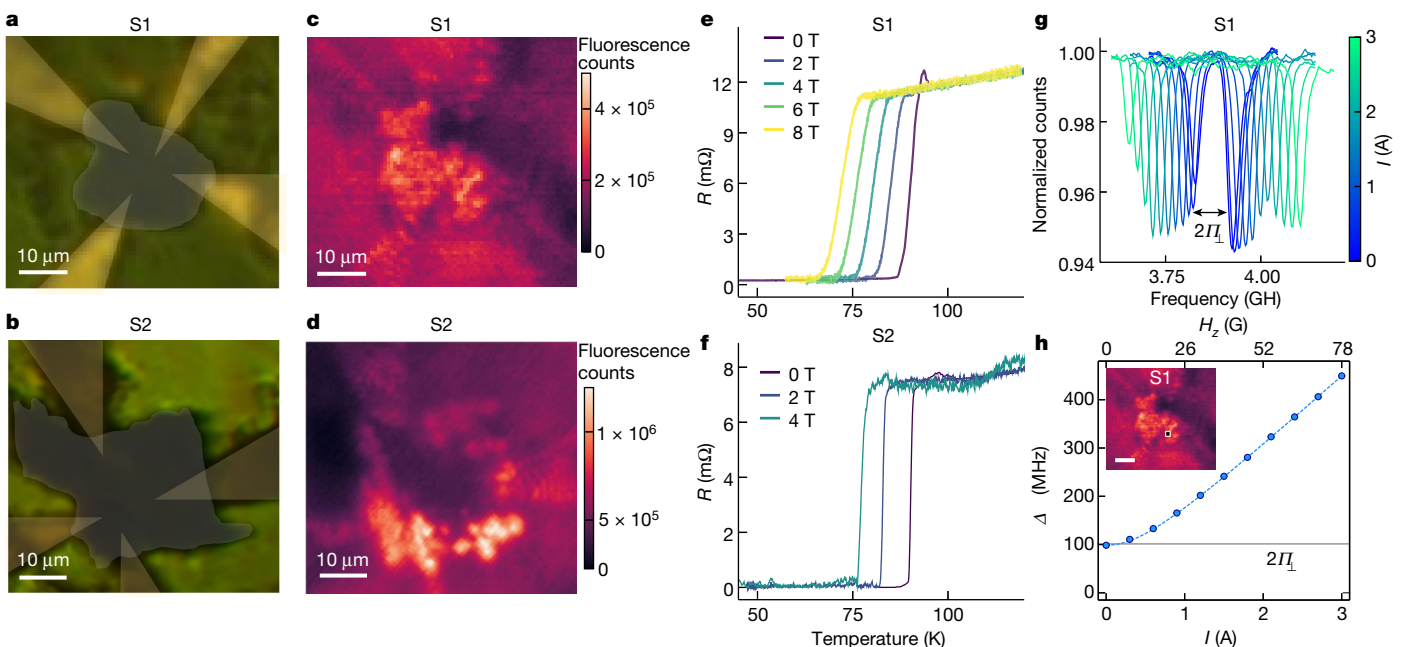


Fig. 2 | Sample synthesis and characterization. To prepare samples S1 and S2, we compress a mixture of cerium (Ce) metal and ammonia borane (NH_3BH_3) to pressures greater than 100 GPa and laser heat (to around 1,500 K) to synthesize cerium hydride. **a,b**, White light microscope images of S1 (**a**) and S2 (**b**) highlighting the Ce metal (grey) and transport leads (yellow). **c,d**, Confocal NV fluorescence maps of the corresponding regions in S1 (**c**) and S2 (**d**) also show the sample and the leads. Bright regions on the Ce metal in S1 and around the Ce metal in S2 correspond to additional NV centres that are created by laser heating (Methods). **e,f**, Electrical resistance measurements of both S1 (118 GPa, **e**) and S2 (137 GPa, **f**) exhibit a sharp drop, with $T_c(P) \approx 90$ K, suggesting the formation of CeH_0 (ref. 10). T_c is suppressed on the application of magnetic

fields. **g,h**, Calibration of the applied field, H_z , at room temperature ($T = 300$ K). We generate the field, H_z , by applying a current, I , in an electromagnet. Starting with a stress-induced splitting $2\Pi_{\perp}$ at $I = 0$, we measure an increase in the ODMR splitting, Δ , with increasing current. ODMR spectra (**g**) measured for different values of I at a specific spatial point on sample S1 (**h**, inset). The ODMR splitting $\Delta = \sqrt{(2\Pi_{\perp})^2 + (2\gamma_B B_z)^2}$ is a quadrature sum of the stress splitting, $2\Pi_{\perp} \approx (2\pi) \times 98$ MHz, and the Zeeman splitting, $2\gamma_B B_z$. In the absence of sample magnetism (that is, for $T > T_c$), $B_z = H_z \propto I$. Fitting the measured splitting Δ to this functional form (**h**), we directly extract H_z (in gauss), calibrated for each value of I (in amperes). Scale bar, 10 μm (**a–d** and **h**, inset).

provides a simple prescription for measuring B_z : extract Δ from the ODMR spectrum of the NV and then subtract (in quadrature) the stress-induced splitting, $2\Pi_{\perp}$, measured at zero field.

Although conceptually simple, extending this approach to megabar pressures^{39,40} has been subject to persistent challenges. These include diminishing NV fluorescence, significant broadening of the ODMR spectrum and a marked loss of optical contrast above approximately 50 GPa (ref. 36). We address these difficulties by introducing an approach to NV-based metrology at megabar pressures. In particular, by using a [111]-cut anvil, we engineer the dominant culet stress to project along the quantization axis for one specific subgroup of NV centres (Fig. 1b). Doing so has been conjectured to reduce the loss of contrast at high pressures^{41,42} (Methods). This is borne out by the data shown in Fig. 1d—the ODMR contrast for NVs in a [111]-cut anvil is two orders of magnitude larger than that in a [100]-cut anvil. This enables us to characterize both continuous-wave and pulsed measurements up to pressures of the order of about 140 GPa. For continuous-wave measurements, we achieve a maximum of about 15% contrast at megabar pressures, roughly an order of magnitude larger than that obtained under quasi-hydrostatic stresses in previous micro diamond studies³⁹. This leads to typical magnetic field sensitivities of around 35 μT Hz^{-1/2} (Methods). For pulsed measurements, we perform a spin echo and measure a coherence time, $T_2^{\text{echo}} = 2.04(4)$ μs at 137 GPa (Fig. 1e).

Let us now calibrate the external magnetic field at megabar pressure. The field strength is tuned by the current, I , applied to an electromagnet; Fig. 2g shows the ODMR spectra of sample S1 at room temperature ($T = 300$ K) as the applied current is increased. By extracting the ODMR splitting Δ at each value of the current, and then subtracting the $2\Pi_{\perp}$ splitting measured at $I = 0$, we can immediately convert the applied current to an external magnetic field strength, H_z (Fig. 2h). This conversion

assumes that the CeH_0 sample does not contribute an appreciable additional field above the superconducting transition temperature and that $B_z = H_z$ (in Gaussian units). We verify the robustness of this assumption by confirming that H_z is independent of both the temperature and the spatial location within the sample chamber (Methods). Furthermore, we note that sample S2 yields the same current-to-field calibration.

Local suppression of an external field

To probe the magnetic response of the sample below T_c , we perform NV magnetometry in a cryogenic system (down to $T = 25$ K) integrated with a scanning confocal microscope (Methods). Beginning with sample S2 at 300 K, we perform zero-field cooling (at $P = 137$ GPa) below the transition temperature ($T_c \approx 91$ K) to $T = 81$ K and perform ODMR spectroscopy at several points within the sample chamber. We focus on two representative spatial points: one above the CeH_0 sample (Fig. 3d, green point) and the other far from the sample (Fig. 3d, purple point). Starting with the distant point, at $H_z = 0$, we find that the NV exhibits a $2\Pi_{\perp}$ splitting of about $(2\pi) \times 134$ MHz (Fig. 3a, light blue curve). As expected, turning on the external magnetic field (up to $H_z = 70$ G) causes the spectrum to further split (Fig. 3a, darker blue curves). We extract the magnetic field, B_z , at the location of the NV as a function of the external applied field, H_z , and find that $B_z = H_z$ nearly perfectly (Fig. 3e, purple data). This implies that away from the CeH_0 sample, there is no local magnetization.

The response of NVs above the CeH_0 is markedly distinct. The ODMR splitting, Δ , exhibits a significantly weaker increase as the external field is ramped up (Fig. 3b), indicative of a local suppression in B_z (Fig. 3e, green points). This response is consistent with diamagnetism from the sample as would be expected from a superconducting Meissner effect. A similar local suppression is observed in sample S1 (Fig. 3f).

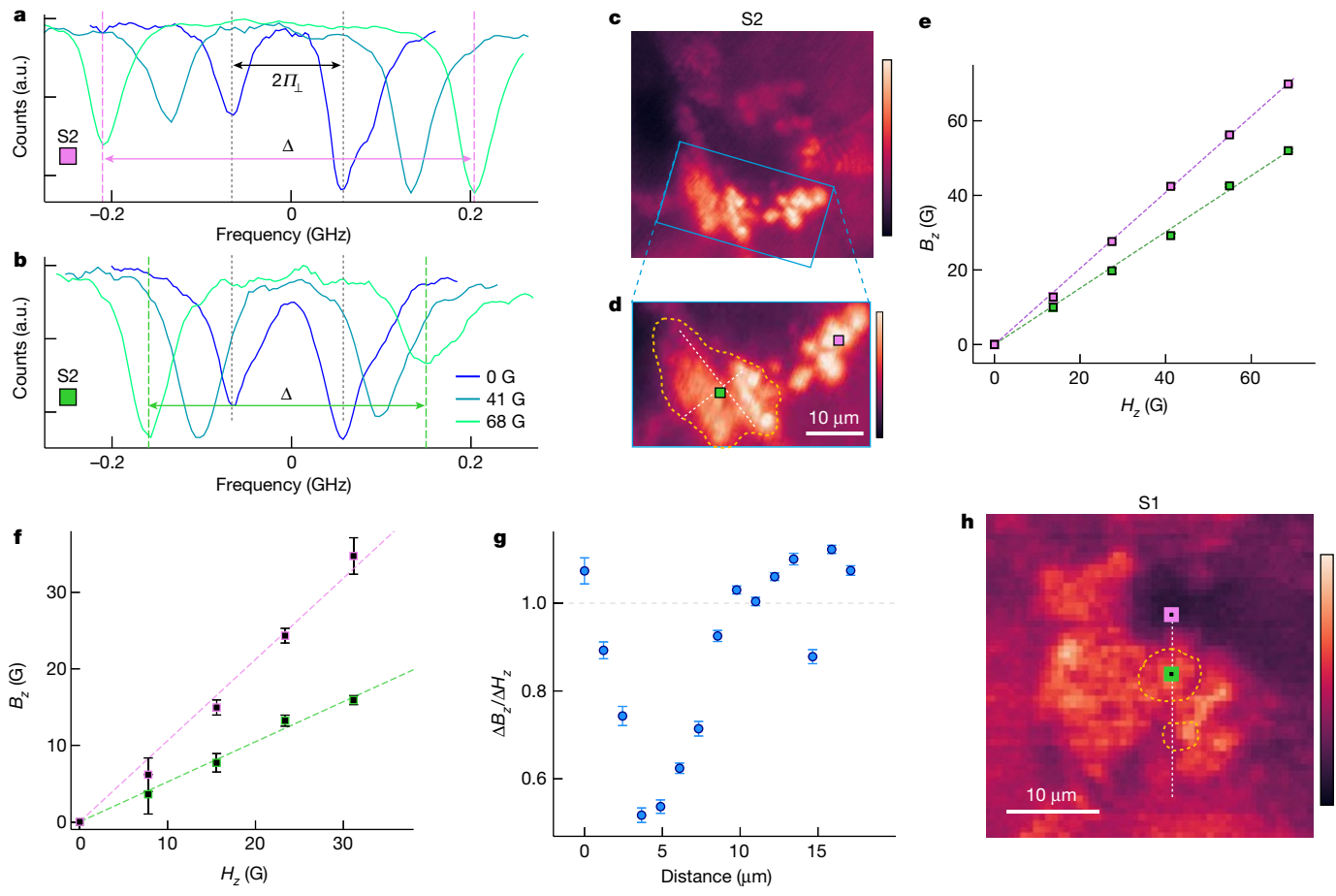


Fig. 3 | Local diamagnetism in CeH₀. **a,b**, ODMR spectra collected on zero-field cooling to a temperature $T < T_c$, at two representative spatial points in sample S2 (shown in **d**). The purple point **a** is far from the CeH₀ sample, whereas the green point in **b** is directly above it. As H_z is increased (at $T = 81), the ODMR splitting above the CeH₀ (**b**) is suppressed relative to the splitting away from it (**a**). For clarity, all spectra have been centred by subtracting the ODMR shift. **c**, Confocal fluorescence image of S2. **d**, By performing ODMR at different spatial points, we identify a sub-region of extent of about 10 μm exhibiting local diamagnetism (delineated by the dotted yellow line in **d**). We use this signal to identify the regions in which CeH₀ has been successfully synthesized. **e**, For the purple point sitting outside this sub-region and for the green point sitting inside this sub-region ($T = 81\text{ K}$), we plot B_z extracted from$

the ODMR spectra (**a,b**) at each value of H_z . Away from the CeH₀ (purple), we measure a slope $s = \Delta B_z / \Delta H_z = 1.02$, suggesting that there is no local magnetization. By contrast, above the CeH₀ (green), we measure a slope $s = 0.75$, demonstrating a clear local suppression of the external magnetic field ($B_z < H_z$), consistent with the Meissner effect. **f**, We perform analogous measurements at $T = 25\text{ K}$ in sample S1 (green and purple points in **h**). In comparison with S2, we observe a stronger suppression ($s = 0.52$) above the CeH₀. **g**, By measuring the slope $s = \Delta B_z / \Delta H_z$ at $T = 25\text{ K}$ along a line cut (dotted white line in **h**, with distance measured from top to bottom) we image the spatial profile of the magnetic field suppression in sample S1. **h**, We identify two disconnected sub-regions of an extent greater than 10 μm exhibiting local diamagnetism (that is, $s < 1$). a.u., arbitrary units. Scale bar, 10 μm (**c,d** and **h**).

Our ability to locally image the diamagnetic response enables us to directly characterize the geometry and size of the superconducting regions within the sample chamber. As an example, Fig. 3g shows a particular line cut in sample S1. For each point along the line cut, we measure B_z as a function of H_z and extract the slope, $s = \Delta B_z / \Delta H_z$, where $s < 1$ indicates suppression of the local field. As shown in Fig. 3g, there exists a contiguous region in which $s < 1$, suggesting the presence of an approximately 7–10- μm -sized region of superconducting CeH₀. Similar-sized regions of CeH₀ are also observed in sample S2 (see, for example, the orthogonal line cuts indicated in Fig. 3d and Methods). Our spatial surveys point to an important observation: although synthesis is performed by rastering a high-power laser, only a fraction of the laser-heated area exhibits superconductivity.

Simultaneous magnetometry and resistance

Focusing on sample S2, we now characterize the local field suppression as a function of increasing temperature. In particular, we follow the experimental sequence shown in Fig. 4a (black and red curves): We

begin by performing zero-field cooling of the sample below T_c , then we ramp up an external magnetic field, and finally, fixing this field ($H_z = 79\text{ G}$), we slowly increase the temperature above T_c . During the field-heating sequence, we measure both four-terminal resistance and the ODMR spectrum of the NV (Fig. 4d). The resistance exhibits a jump at $T_c \approx 91\text{ K}$. The behaviour of the local magnetic field measured by the NV centres is more subtle^{8,43} (Fig. 4c,d). In particular, for temperatures $T < 72\text{ K}$, the local field B_z exhibits a plateau at about 53 G, significantly below the value of the external applied field, $H_z = 79\text{ G}$. For intermediate temperatures, $73\text{ K} < T < 90\text{ K}$, B_z exhibits a slow increase, suggesting a gradual weakening of diamagnetism. Finally, for temperatures $T > 91\text{ K}$, coincident with the superconducting transition measured by resistance, B_z exhibits a second plateau in agreement with the strength of the external magnetic field.

Partial field expulsion on field cooling

Although we have observed clear signatures of diamagnetism after zero-field cooling, a complementary signature of a superconductor

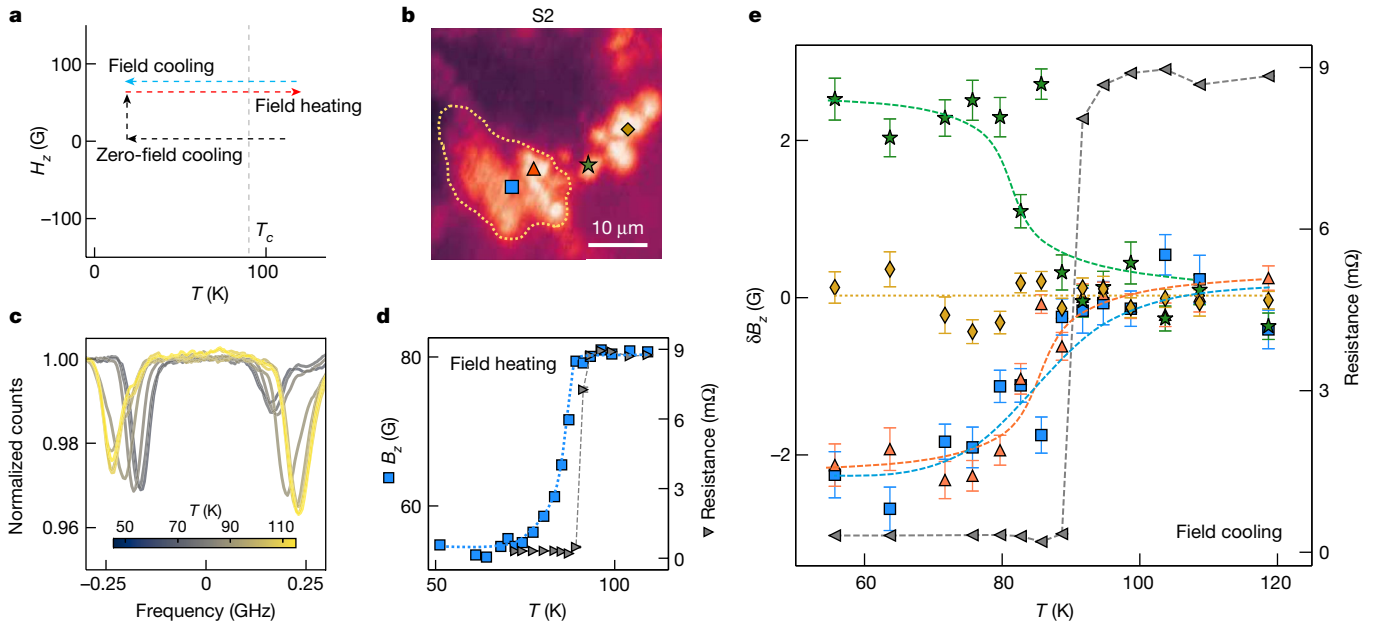


Fig. 4 | Simultaneous measurements of electrical resistance and magnetism on sweeping T . **a**, Schematic of experimental protocols. **b**, Confocal fluorescence image of S2 magnified into the same CeH_9 region as Fig. 3d. NV ODMR spectroscopy is performed at four spatial points: two points above the CeH_9 region (blue and red), one point at the edge of this region (green) and one point far away from this region (yellow). **c**, NV ODMR spectra collected at the blue spatial point in **b** on field heating at $H_z = 79$ G (following zero-field cooling). The ODMR splitting Δ increases as T is increased across T_c .

d, The local field, B_z (left y-axis), extracted from the ODMR splitting Δ shown in **c**. The four-point resistance (right y-axis) is measured simultaneously. **e**, Simultaneous measurements of four-point resistance (right y-axis) and the change in the local field, δB_z (left y-axis), at the four spatial points in **b** on field cooling with $H_z = 79$ G. The measured resistance identifies a clear transition at $T_c \approx 91$ K. At each spatial point, we determine δB_z relative to the average value of the measured B_z in the normal state (that is, for temperature $T > 91$ K). Scale bar, 10 μm (**b**).

is the ability to expel magnetic flux on field cooling⁴⁴ (Fig. 4a, blue arrow). We simultaneously measure the resistance and perform ODMR spectroscopy (during field cooling) at four spatial points on sample S2 (Fig. 4b): a pair of points (red and blue) above the identified CeH_9 region (enclosed by the dotted yellow line), a point (green) just outside the CeH_9 region and a point (yellow) far away from the CeH_9 region. Again, the resistance exhibits a sharp transition at about 91 K (Fig. 4e, grey triangles, right y-axis). At each spatial point, we determine the change in the local field, δB_z , across this transition relative to the average B_z measured in the normal state ($T > 91$ K) (Fig. 4e, left y-axis). Far from the CeH_9 region (yellow), the local field is temperature independent across the transition. Above the CeH_9 region (red and blue), the local field decreases by around 2 G on cooling below the transition. Near the edge of the CeH_9 region (green), the local field, B_z , increases by approximately 2 G. Taken together, these observations are consistent with partial flux expulsion: as the sample is cooled below T_c , it expels magnetic flux from the CeH_9 region, leading to a reduction in the magnetic flux directly above the sample and a concentration at the edge.

We note that the qualitative profiles of B_z above the CeH_9 region on field heating (Fig. 4d) and field cooling (Fig. 4e) are remarkably similar. However, the quantitative values are quite distinct: the strength of the local field expulsion (on field cooling) is an order of magnitude weaker than the strength of the local field suppression (after zero-field cooling). This suggests that during field cooling, the external magnetic field is able to partially penetrate through the sample (Fig. 5b), an observation consistent with previous measurements on superhydrides²⁷. Associated with the penetration of magnetic flux on field cooling is the possibility of flux trapping—a textbook signature of disordered superconductors in which the disorder ‘pins’ the permeating magnetic field (Methods). This pinning leads to a remnant magnetic field, arising from frozen-in magnetic moments within the superconductor, even when the applied external field is quenched ($H_z \rightarrow 0$ G) after field cooling^{45,46}.

Flux trapping and hysteresis

To investigate the presence of flux trapping, we examine three spatial points above the CeH_9 region in sample S2 (Fig. 5c, blue, white and red points). After field cooling the sample at $H_z = 103$ G, we quench the external magnetic field to zero. The resulting ODMR spectra for one of the three spatial points (Fig. 5c, white point) are shown in Fig. 5(a) (dark blue curve). By comparing with the zero-field cooled spectrum at the same spatial point (Fig. 5a, light blue curve), we find that the ODMR splitting, Δ , shows the presence of a remnant 34 G field, despite the fact that the external field H_z is 0 G. This is precisely the expected signature of flux trapping. The same signature is observed at the other two spatial points (Methods).

To further explore this flux trapping, we follow the experimental sequence shown in Fig. 5e; in particular, after field cooling at $H_z = 103$ G to a fixed temperature $T < T_c$, we ramp the external field down to $H_z = -154$ G, and then back up to $H_z = +154$ G. For a temperature ($T = 66$ K) well below the transition temperature ($T_c \approx 91$ K), as the external field is ramped down, B_z decreases but reaches a finite (flux-trapped) value of about 34 G at $H_z = 0$ G. As the external field switches direction ($H_z < 0$ G), B_z continues to decrease, reaching zero at $H_z \approx -51$ G; this is consistent with competition between the external magnetic field and the flux-trapped field from CeH_9 . At even larger magnitudes of negative H_z , B_z also becomes negative and scales with H_z . Finally, as we ramp back up to positive H_z fields, we observe no hysteresis in the measured B_z (Fig. 5f).

A few remarks are in order. First, as a benchmark, we perform the same set of experiments (Fig. 5e) for a spatial point outside the CeH_9 region, and always observe $B_z = H_z$ (Extended Data Fig. 8f). Second, the data in Fig. 5f exhibit a slope, $s \approx 0.67$, indicating the presence of local field suppression; this slope is in quantitative agreement with that obtained on applying a magnetic field after zero-field cooling (at the same spatial location; Methods). Despite the trapped flux, the sample

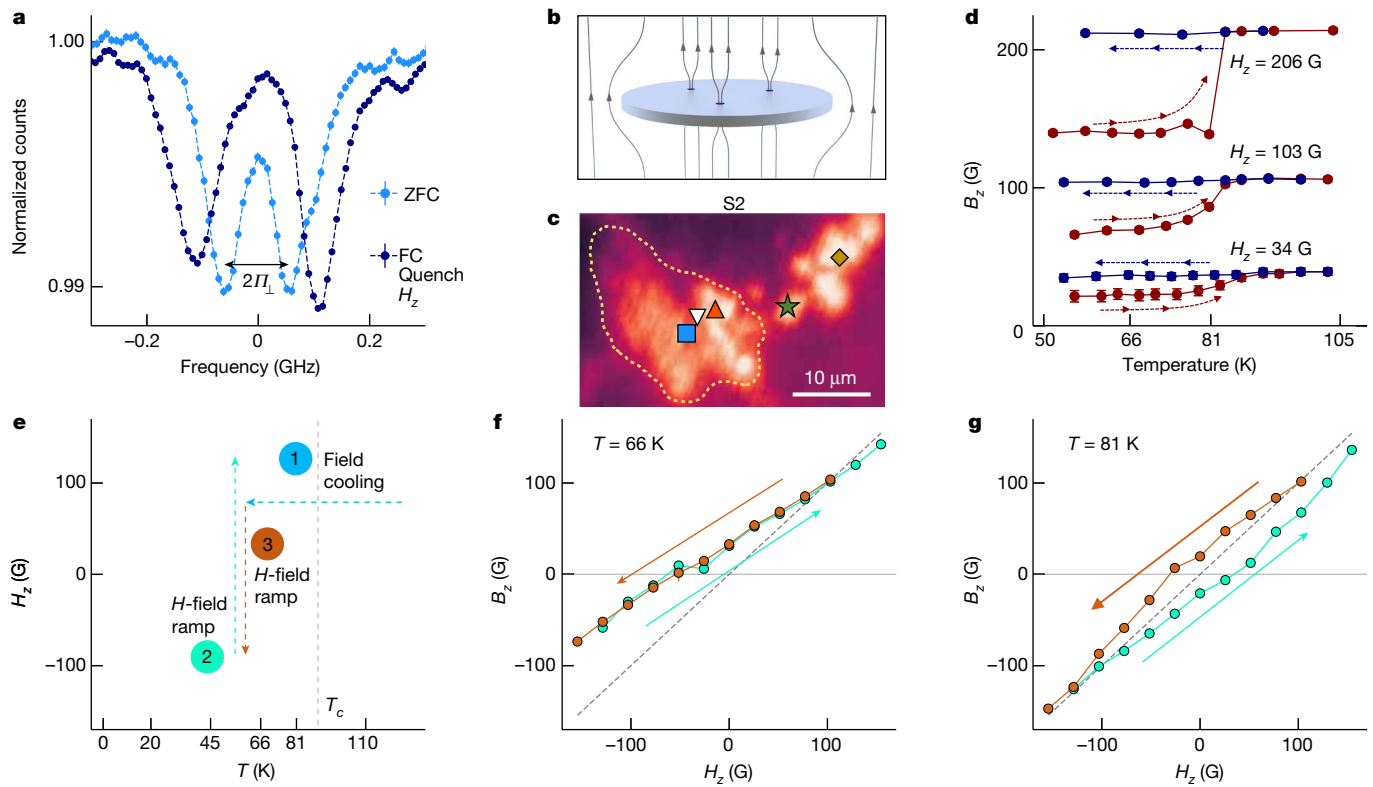


Fig. 5 | Flux trapping and hysteresis in CeH₉. **a**, Comparison of ODMR spectra at $H_z = 0$ G, which are collected at the white spatial point in **c**. The light blue data are obtained after zero-field cooling (ZFC), whereas the dark blue data are measured after field cooling (FC) (at $H_z = 103$ G) and subsequently quenching H_z . **b**, Schematic showing the penetration of external magnetic flux through the superconducting sample. **c**, Confocal fluorescence image of S2 magnified into the same CeH₉ region as in Fig. 3d. All data in this figure are collected at the white spatial point. **d**, Measurements of B_z for the full experimental sequence shown in Fig. 4a on ramping to three different values of H_z . **e–g**, Measurements of hysteresis on sweeping H_z at fixed T . Schematic of the experimental sequence (**e**). In the absence of any local magnetization, we expect $B_z = H_z$ (dotted grey line in **f,g**). Fixing $T = 66$ K (deep in the superconducting phase) (**f**), we measure a

flux-trapped field ($B_z = +34$ G at $H_z = 0$ G) and no appreciable hysteresis on sweeping H_z . The measured slope $s = \Delta B_z / \Delta H_z \approx 0.67 < 1$ agrees perfectly with that measured after zero-field cooling for this same spatial point (Methods). By contrast, fixing $T = 81$ K (near T_c) (**g**) and sweeping H_z , we observe clear hysteresis. On ramping to $H_z \approx -100$ G, the measured B_z is nearly the same as the applied field H_z , without any observed change in the electrical resistance. On ramping back up to $H_z = 0$ G, we observe a flux-trapped field in the opposite direction ($B_z = -23$ G). Assuming the flux-trapped field originates from vortices pinned within CeH₉ (refs. 44,46), we find that an applied field of $H_z = -154$ G is not strong enough to de-pin the vortices at $T = 66$ K but is at $T = 81$ K, leading to the observed hysteresis. Scale bar, 10 μm (**c**).

exhibits a diamagnetic response similar to that observed on zero-field cooling. This suppression also helps to explain the following observation: Although we detect a remnant flux-trapped field of $B_z \approx 34$ G, we find that this field is cancelled (that is, the NVs measure $B_z = 0$ G) only for an applied field $H_z \approx -51$ G. Finally, we note that the data in Fig. 5f are taken over the course of several days. In combination with the lack of any observed hysteresis, this suggests that the flux-trapped field arises from persistent currents within the CeH₉ sample.

On field cooling to a temperature ($T = 81$ K) near the transition, we observe distinct behaviour in the measured B_z as a function of magnetic field sweeps (Fig. 5g). As the external field is initially ramped down, we observe analogous signatures of flux trapping with $B_z = 20$ G at $H_z = 0$ G. However, as we switch the direction of the external field ($H_z < 0$ G), the slope of the response changes and we find a scaling consistent with $B_z = H_z$ at the largest negative H_z fields. On ramping back up to positive H_z fields, we observe clear hysteresis in the data with signatures of flux trapping in the opposite direction, that is, $B_z = -23$ G at $H_z = 0$ G. Again, as we switch the direction of the external field (back to $H_z > 0$ G), the slope of the response changes, and we find a scaling consistent with $B_z = H_z$ at the largest positive H_z fields. Figure 5f,g suggests that the strength of the flux trapping is temperature dependent⁴⁶. Moreover, as shown in Extended Data Fig. 7, the trapping strength itself exhibits hysteresis: on zero-field cooling to the same temperature, a significantly larger H_z is required before we measure a scaling consistent with $B_z = H_z$.

Finally, we turn to a systematic exploration of hysteresis as a function of temperature sweeps at fixed H_z (experimental sequence; Fig. 4a). We begin by zero-field cooling the sample and then ramping up a magnetic field to various strengths. We measure ODMR spectra as the temperature is increased above T_c (field heating) and then decreased below T_c (field cooling). The resulting data for B_z are shown in Fig. 5d. Two features are apparent in the data. First, the hysteresis between field heating (red) and field cooling (blue) is enhanced at larger H_z fields (Fig. 5d). Second, at $H_z = 206$ G, we observe a surprising sharpening of the magnetic transition (measured by the jump in B_z) compared with that seen at smaller H_z fields.

Discussion and Conclusions

Our demonstration of magnetic imaging up to about 140 GPa with high contrast and minimal stress inhomogeneity opens up a previously unknown range of measurements on materials in the megabar regime, including both d.c. magnetometry and noise spectroscopy⁴⁷. Looking forward, our work provides a lot of opportunities. First, we expect that our NV-based quantum sensing techniques can readily be extended to even higher pressures (that is, ≥ 200 GPa), for example, using double-bevelled anvils. Second, it would be interesting to revisit other high-pressure superconductors, such as LaH₁₀ and H₃S, in which previous magnetic measurements have been limited to global probes,

such as superconducting quantum interference devices (SQUIDs)^{11,45} and pick-up coils^{48,49}. Third, local magnetometry is particularly important for superhydride materials, in which synthesis by laser heating leads to inhomogeneities at the micron scale. Imaging and characterizing these inhomogeneities is a crucial step towards quantifying sample yield and improving synthesis recipes.

Online content

Any methods, additional references, Nature Portfolio reporting summaries, source data, extended data, supplementary information, acknowledgements, peer review information; details of author contributions and competing interests; and statements of data and code availability are available at <https://doi.org/10.1038/s41586-024-07026-7>.

1. Mao, H.-K., Chen, X.-J., Ding, Y., Li, B. & Wang, L. Solids, liquids, and gases under high pressure. *Rev. Mod. Phys.* **90**, 015007 (2018).
2. Wang, D., Ding, Y. & Mao, H.-K. Future study of dense superconducting hydrides at high pressure. *Materials* **14**, 7563 (2021).
3. Lilia, B. et al. The 2021 room-temperature superconductivity roadmap. *J. Phys. Condens. Matter* **34**, 183002 (2022).
4. Zhang, F. & Oganov, A. R. Valence state and spin transitions of iron in Earth's mantle silicates. *Earth Planet. Sci. Lett.* **249**, 436–443 (2006).
5. Loubeyre, P., Occelli, F. & Dumas, P. Synchrotron infrared spectroscopic evidence of the probable transition to metal hydrogen. *Nature* **577**, 631–635 (2020).
6. Weck, G. et al. Evidence and stability field of FCC superionic water ice using static compression. *Phys. Rev. Lett.* **128**, 165701 (2022).
7. Hsieh, S. et al. Imaging stress and magnetism at high pressures using a nanoscale quantum sensor. *Science* **366**, 1349–1354 (2019).
8. Lesik, M. et al. Magnetic measurements on micrometer-sized samples under high pressure using designed NV centers. *Science* **366**, 1359–1362 (2019).
9. Steele, L. G. et al. Optically detected magnetic resonance of nitrogen vacancies in a diamond anvil cell using designer diamond anvils. *Appl. Phys. Lett.* **111**, 221903 (2017).
10. Chen, W. et al. High-temperature superconducting phases in cerium superhydride with a T_c up to 115 K below a pressure of 1 megabar. *Phys. Rev. Lett.* **127**, 117001 (2021).
11. Drozdov, A. P., Eremets, M. I., Troyan, I. A., Ksenofontov, V. & Shylin, S. I. Conventional superconductivity at 203 kelvin at high pressures in the sulfur hydride system. *Nature* **525**, 73–76 (2015).
12. Drozdov, A. P. et al. Superconductivity at 250 K in lanthanum hydride under high pressures. *Nature* **569**, 528–531 (2019).
13. Hong, F. et al. Superconductivity of lanthanum superhydride investigated using the standard four-probe configuration under high pressures. *Chinese Phys. Lett.* **37**, 107401 (2020).
14. Somayazulu, M. et al. Evidence for superconductivity above 260 K in lanthanum superhydride at megabar pressures. *Phys. Rev. Lett.* **122**, 027001 (2019).
15. Kong, P. et al. Superconductivity up to 243 K in the yttrium–hydrogen system under high pressure. *Nat. Commun.* **12**, 5075 (2021).
16. Troyan, I. A. et al. Anomalous high-temperature superconductivity in YH_6 . *Adv. Mater.* **33**, 2006832 (2021).
17. Semenok, D. V. et al. Superconductivity at 161 K in thorium hydride ThH_{10} : synthesis and properties. *Mater. Today* **33**, 36–44 (2020).
18. Zhou, D. et al. Superconducting praseodymium superhydrides. *Sci. Adv.* **6**, eaax6849 (2020).
19. Semenok, D. V. et al. Superconductivity at 253 K in lanthanum–yttrium ternary hydrides. *Mater. Today* **48**, 18–28 (2021).
20. Hong, F. et al. Possible superconductivity at ~ 70 K in tin hydride SnH_x under high pressure. *Mater. Today Phys.* **22**, 100596 (2022).
21. Chen, W. et al. Synthesis of molecular metallic barium superhydride: pseudocubic BaH_{12} . *Nat. Commun.* **12**, 273 (2021).
22. Ma, L. et al. High-temperature superconducting phase in clathrate calcium hydride CaH_6 up to 215 K at a pressure of 172 GPa. *Phys. Rev. Lett.* **128**, 167001 (2022).
23. Li, Z. et al. Superconductivity above 200 K discovered in superhydrides of calcium. *Nat. Commun.* **13**, 2863 (2022).
24. He, X. et al. Superconductivity observed in tantalum polyhydride at high pressure. *Chinese Phys. Lett.* **40**, 057404 (2023).
25. Ashcroft, N. W. Metallic hydrogen: a high-temperature superconductor?. *Phys. Rev. Lett.* **21**, 1748–1749 (1968).
26. Ashcroft, N. W. Hydrogen dominant metallic alloys: high temperature superconductors? *Phys. Rev. Lett.* **92**, 187002 (2004).
27. Eremets, M. I. et al. High-temperature superconductivity in hydrides: experimental evidence and details. *J. Supercond. Nov. Magn.* **35**, 965–977 (2022).
28. Hirsch, J. E. & Marsiglio, F. Absence of magnetic evidence for superconductivity in hydrides under high pressure. *Physica C Supercond. Appl.* **584**, 1353866 (2021).
29. Yip, K. Y. et al. Measuring magnetic field texture in correlated electron systems under extreme conditions. *Science* **366**, 1355–1359 (2019).
30. Gavriluk, A. G., Mironovich, A. A. & Struzhkin, V. V. Miniature diamond anvil cell for broad range of high pressure measurements. *Rev. Sci. Instrum.* **80**, 043906 (2009).
31. Doherty, M. W. et al. The nitrogen-vacancy colour centre in diamond. *Phys. Rep.* **528**, 1–45 (2013).
32. Acosta, V. M. et al. Temperature dependence of the nitrogen-vacancy magnetic resonance in diamond. *Phys. Rev. Lett.* **104**, 070801 (2010).
33. Maze, J. R. et al. Nanoscale magnetic sensing with an individual electronic spin in diamond. *Nature* **455**, 644–647 (2008).
34. Dolde, F. et al. Electric-field sensing using single diamond spins. *Nat. Phys.* **7**, 459–463 (2011).
35. Ovartchaiyapong, P., Lee, K. W., Myers, B. A. & Jayich, A. C. B. Dynamic strain-mediated coupling of a single diamond spin to a mechanical resonator. *Nat. Commun.* **5**, 4429 (2014).
36. Doherty, M. W. et al. Electronic properties and metrology applications of the diamond NV-center under pressure. *Phys. Rev. Lett.* **112**, 047601 (2014).
37. Barson, M. S. J. et al. Nanomechanical sensing using spins in diamond. *Nano Lett.* **17**, 1496–1503 (2017).
38. Schirhagl, R., Chang, K., Loretz, M. & Degen, C. L. Nitrogen-vacancy centers in diamond: nanoscale sensors for physics and biology. *Annu. Rev. Phys. Chem.* **65**, 83–105 (2014).
39. Dai, J.-H. et al. Optically detected magnetic resonance of diamond nitrogen-vacancy centers under megabar pressures. *Chinese Phys. Lett.* **39**, 117601 (2022).
40. Hilberer, A. et al. Enabling quantum sensing under extreme pressure: Nitrogen-vacancy magnetometry up to 130 GPa. *Phys. Rev. B* **107**, L220102 (2023).
41. Goldman, M. L. et al. State-selective intersystem crossing in nitrogen-vacancy centers. *Phys. Rev. B* **91**, 165201 (2015).
42. Davies, G. & Hamer, M. Optical studies of the 1.945 eV vibronic band in diamond. *Proc. R. Soc. Lond. A Math. Phys. Sci.* **348**, 285–298 (1976).
43. Nusran, N. et al. Spatially-resolved study of the Meissner effect in superconductors using NV-centers-in-diamond optical magnetometry. *New J. Phys.* **20**, 043010 (2018).
44. Tinkham, M. *Introduction to Superconductivity* (Courier, 2004).
45. Minkov, V. S., Ksenofontov, V., Bud'ko, S. L., Talantsev, E. F. & Eremets, M. I. Magnetic flux trapping in hydrogen-rich high-temperature superconductors. *Nat. Phys.* **19**, 1293–1300 (2023).
46. Matsushita, T. et al. *Flux Pinning in Superconductors*, Vol. 164 (Springer, 2007).
47. Xu, Y., Zhang, W. & Tian, C. Recent advances on applications of NV magnetometry in condensed matter physics. *Photon. Res.* **11**, 393–412 (2023).
48. Huang, X. et al. High-temperature superconductivity in sulfur hydride evidenced by alternating-current magnetic susceptibility. *Natl. Sci. Rev.* **6**, 713–718 (2019).
49. Struzhkin, V. et al. Superconductivity in La and Y hydrides: remaining questions to experiment and theory. *Matter Radiat. Extrem.* **5**, 028201 (2020).

Publisher's note Springer Nature remains neutral with regard to jurisdictional claims in published maps and institutional affiliations.

Springer Nature or its licensor (e.g. a society or other partner) holds exclusive rights to this article under a publishing agreement with the author(s) or other rightsholder(s); author self-archiving of the accepted manuscript version of this article is solely governed by the terms of such publishing agreement and applicable law.

© The Author(s), under exclusive licence to Springer Nature Limited 2024

Article

Methods

Electrical resistance and magnetism in CeH_x

Local diamagnetism in S1. In the main text, we show the ODMR spectra and extracted B_z values for our study of sample diamagnetism on zero-field cooling of sample S2 (Fig. 3a,b,e). We also show the extracted B_z values for sample S1 (Fig. 3f). Here, we include the ODMR spectra (Extended Data Fig. 1b,c) that were used in the extraction of B_z at the relevant spatial locations in S1 (Extended Data Fig. 1a, green and purple points).

Order of magnitude estimation. The NV centres can measure only the magnetic field, B_z , outside the CeH_x sample; therefore, we cannot, in principle, directly measure the zero-field condition inside the superconductor (Meissner effect). Rather, we can measure only a diamagnetic suppression in the local field. Furthermore, owing to the presence of micron-scale inhomogeneities, it is complicated to accurately model the field inside the superconductor. Nevertheless, we can estimate the strength of the diamagnetic response of the sample and compare this with conventional metallic diamagnets.

For this simple estimate, we consider a spherical sample of radius R with the NV centres located directly below the sample at a distance r from the centre (Extended Data Fig. 3d). On the application of an external field, H_z , the sample exhibits a magnetization $M_z = \chi H_z$, where χ is the magnetic susceptibility. We note that for a perfect diamagnet (Meissner effect), $\chi = -1/4\pi$ resulting in $\mathbf{B} = \mathbf{H} + 4\pi\mathbf{M} = 0$ inside the superconductor. Consequently, the overall dipole moment of the sample is $d = \frac{4\pi}{3}MR^3$. Directly below the sample, the local field $B_z = H_z + \frac{3}{4\pi}d/r^3 = H_z(1 + 4\pi\chi(R/r)^3)$. This results in a slope $s = dB_z/dH_z = (1 + 4\pi\chi(R/r)^3)$. Within the assumed geometry, this enables us to directly estimate the magnetic susceptibility of the sample, $|\chi| = \frac{|1-s|}{4\pi}(r/R)^3$, from our measurements of $s \approx 0.5$ for sample S1 and $s \approx 0.7$ for sample S2 in the main text. Given that $r > R$, we find that $|\chi| > 0.5/4\pi$ for sample S1 and $|\chi| > 0.3/4\pi$ for sample S2; these values are significantly larger than those expected from metallic diamagnets such as bismuth⁵⁰ and reasonably consistent with the expected magnitude of χ for a perfect diamagnet.

Conversely, assuming a perfect diamagnetic response ($\chi = -1/4\pi$), we show that the sample-probe geometry is also consistent for the current experiment. Although NV centres were directly implanted approximately 50 nm below the culet surface, as shown in Supplementary Fig. 3, the laser heating (during the CeH_x synthesis process) creates additional NV centres up to about less than 1 μm below the culet surface, and it is these NV centres that we believe dominate the ODMR signal. Assuming a perfect diamagnet with $\chi = -1/4\pi$, we find that the slope should be $s = dB_z/dH_z = (1 - (R/r)^3)$. In our experiments, we measure $s \approx 0.5$ for sample S1 and $s \approx 0.7$ for sample S2. Based on these measurements, we would estimate $r \approx 1.3R$ for sample S1 and $r \approx 1.5R$ for sample S2. Given that our imaging suggests the presence of superconducting CeH_x regions of micron extent and laser-heating-created NVs up to about 1 μm below the culet surface, these values of r are consistent with an external (that is, outside of the sample) measurement of the perfect diamagnetism arising from a superconducting sample with micron-scale inhomogeneities.

Spatial studies of S1 and S2. In the main text, we show a spatially varying local suppression of the external field H_z (Fig. 3g) measured along a line cut in sample S1. Here we include plots of B_z as a function of H_z at several spatial points along this line cut (Extended Data Fig. 2b). We present the same study for two orthogonal line cuts on the CeH_x region of sample S2 (Extended Data Fig. 3).

For spatial studies of local diamagnetism in S1 (Extended Data Fig. 2), we recorded minor spatial drifts in our measurement apparatus. As a result, several ODMR spectra measured for $H_z = 0$ could not be reliably fit to extract the stress splitting, $2\Gamma_{\perp}$. To ensure consistent analysis for

this data set, we determine $2\Gamma_{\perp}$ by a complementary technique. Specifically, at each spatial point, we first fit the measured splitting, Δ , to the function $\Delta = \sqrt{(2\Gamma_{\perp})^2 + (2cl)^2}$, where l is the current applied to the electromagnet and (Γ_{\perp}, c) are fitting parameters. We use this fitted $2\Gamma_{\perp}$ value to extract the local field, B_z , as a function of the applied field H_z in S1. A comparison of the values of B_z extracted using this technique with the values extracted using our prescription (given in the main text) for similar studies in sample S2 does not show any significant differences.

Temperature sweep in S1. In the main text, we present our studies of the magnetic response of sample S2 on zero-field cooling and field cooling (Fig. 4). In particular, we perform NV magnetometry and four-point resistance measurements simultaneously to see concurrent transitions in electrical transport and magnetism across T_c . Here we show our studies of sample S1, in which we perform NV magnetometry and resistance measurements separately (Extended Data Fig. 1d,e). Owing to the coupling between the Pt wire for microwave delivery and the transport leads, accurate determination of four-point resistance on S1 is possible only when the Pt wire is disconnected from the microwave circuitry. We measure a difference of about 9 K between the magnetic transition (Extended Data Fig. 1e, green data) and the resistive transition (Extended Data Fig. 1e, grey data). This difference may be because of a change in the temperature gradient between the DAC and the cold finger on isolating the sample from the microwave circuitry.

Field cooling and hysteresis in S2. In the main text, we show four-point electrical resistance measurements and the change in the local field, δB_z , at four spatial locations in sample S2 on field cooling at $H_z = 79$ G (Fig. 4e). We determine δB_z at each spatial point by subtracting the mean B_z measured at the corresponding location in the normal state (that is, for all temperature points $T > 91$ K). Here we show the ODMR splitting, Δ , and the extracted local field, B_z , measured at these four spatial locations for the same experiment (Extended Data Fig. 4). On top of the synthesized CeH_x region, we measure a decrease in Δ by about $(2\pi) \times 15$ MHz and in B_z by about 2 G on cooling below the transition point, T_c . At the edge of this region, we measure an increase in Δ by about $(2\pi) \times 15$ MHz and in B_z by about 2 G across the transition point. Finally, away from this region we do not measure an appreciable change in Δ or B_z across the transition. At each spatial location, we extract B_z from Δ by using the $2\Gamma_{\perp}$ stress splitting (measured at the respective location at $H_z = 0$ G after zero-field cooling to $T = 86$ K). In the normal state ($T > T_c$), we find systematic differences between the applied field, $H_z \approx 79$ G, and the extracted values of B_z . These may be because of changes in stress splitting, $2\Gamma_{\perp}$, with temperature. Furthermore, they can also stem from any inaccuracy in the determination of $2\Gamma_{\perp}$ because of spatial drift in the sample. Despite these differences, we observe a clear signal in the ODMR splitting, Δ , suggesting flux expulsion within the CeH_x region.

For sample S2, we also study flux trapping on field cooling (at $H_z = 103$ G) to several temperatures $T < T_c$ (Extended Data Fig. 5). We measure the ODMR splitting Δ as a function of H_z . On ramping down to $H_z = 0$, we measure $\Delta > 2\Gamma_{\perp}$ (Extended Data Fig. 5a,d,g,j,m) suggesting the presence of a remnant magnetic field at the location of the NV centre because of flux trapping. By sweeping both magnitude and direction of the external field, we characterize the hysteresis of the trapped flux. In particular, we observe a minimum in the ODMR splitting ($\Delta \approx 2\Gamma_{\perp}$) for $H_z < 0$, where the external field is anti-aligned to the flux-trapped field. On ramping H_z to larger negative values, the splitting increases because the external field dominates the flux-trapped field (Extended Data Fig. 5b,e,h,k,n). Although we can extract only the absolute value of the local field, $|B_z|$, from Δ , we can clearly designate a sign (direction) to B_z based on the continuity in the splitting profile (Extended Data Fig. 5c,f,i,l,o). We find that the hysteresis increases with temperature. Furthermore, deep in the superconducting phase ($T = 61$ K and $T = 66$ K) we measure a slope $s = dB_z/dH_z$ equal to that measured on zero-field

cooling and ramping H_z (Extended Data Fig. 6). This suggests that on field cooling, the sample exhibits an additional response on top of flux trapping. This response is similar to that exhibited on zero-field cooling, in which the sample suppresses the local field.

We study the effect of field cooling at several spatial locations in sample S2 (Extended Data Fig. 8). We find similar signatures of flux trapping at two spatial points on top of the CeH_x region (Extended Data Fig. 8a,b,d,e). At a spatial point away from the sample, we do not observe a magnetic response on field cooling or on zero-field cooling (Extended Data Fig. 8c,f).

Flux penetration in S2 on zero-field cooling and field cooling. In our study of hysteresis of the trapped flux for a temperature close to T_c ($T = 81$ K shown in Extended Data Fig. 5n,o), we measure an overall inversion of the flux-trapped field on ramping H_z . Specifically, after ramping to a field $H_z \approx -154$ G at $T = 81$ K, we find the flux-trapped field is inverted (that is, $B_z < 0$ on returning to $H_z = 0$ G) (Extended Data Fig. 7a). Here we conduct a complementary study of the response of the sample to H_z sweeps after zero-field cooling in which there should be no flux initially trapped. Specifically, we perform zero-field cooling to $T = 81$ K and study the response on ramping the magnitude and direction of H_z . We find that diamagnetic suppression dominates for fields $|H_z| \lesssim 154$ G, and there is no appreciable penetration of flux lines into the sample (Extended Data Fig. 7b). However, on ramping to larger fields ($|H_z| \approx 240$ G) after zero-field cooling to $T = 81$ K (Extended Data Fig. 7c), we observe the penetration and trapping of external flux into the sample (that is, we measure $B_z \neq 0$ on ramping back to $H_z = 0$). Our observations suggest that the penetration of external flux depends on the amount of flux initially trapped in the sample.

Hysteresis on T sweeps in S2. We include the full data set of our study of hysteresis of diamagnetism in S2 on sweeping sample temperature, T , at a fixed value of the external field, H_z . We observe a characteristic loss of suppression on field heating across T_c concurrent with a jump in the four-point resistance. We observe a sharpening of the magnetic transition at the highest field ($H_z = 206$ G in Extended Data Fig. 9d). A repeated measurement along the transition profile for field heating at $H_z = 206$ G (Extended Data Fig. 9d, orange squares) further verifies this observation.

Comparison with SQUID magnetometry at high pressure. Magnetic measurements of high-pressure superhydrides typically rely on SQUID magnetometry in which the dipole sensitivity is of the order of about 10^{-8} emu Hz^{-1/2} (refs. 11,27,45,51). Although expected signals from superhydride samples beat this threshold, the subtraction of

parasitic pick up from a paramagnetic background constitutes an enormous challenge. Moreover, by averaging over the entire DAC geometry, these global probes discard local spatial information of superconducting samples. We demonstrate continuous-wave ODMR spectroscopy, with typical magnetic sensitivity of about 35 μ T Hz^{-1/2} at room temperature. Following previous work, this corresponds to a dipole sensitivity of the order of about 10^{-11} emu Hz^{-1/2} at room temperatures (around 10^{-10} emu Hz^{-1/2} at cryogenic temperatures)⁷. In this case, a key advantage is the proximity of the sensor to the target material and the ability to measure magnetism with diffraction-limited sub-micron spatial resolution.

Data availability

The published data of this study are available on the Zenodo public database (<https://doi.org/10.5281/zenodo.8219843>).

50. Focke, A. B. The principal magnetic susceptibilities of bismuth single crystals. *Phys. Rev.* **36**, 319–325 (1930).
51. Minkov, V. S. Magnetic field screening in hydrogen-rich high-temperature superconductors. *Nat. Commun.* **13**, 3194 (2022).

Acknowledgements This work was supported as part of the Center for Novel Pathways to Quantum Coherence in Materials, an Energy Frontier Research Center funded by the US Department of Energy, Office of Science, Basic Energy Sciences under award no. DE-AC02-05CH1231. X.H. acknowledges support from the National Key R&D Program of China (grant no. 2022YFA1405500). C.R.L. acknowledges support from the National Science Foundation (grant no. PHY-1752727). M.B. acknowledges support from the Department of Defense through the National Defense Science and Engineering Graduate Fellowship Program. S.H. and S.M. acknowledge support from the National Science Foundation Graduate Research Fellowship under grant no. DGE-1752814. N.Y.Y. acknowledges support from the David and Lucile Packard Foundation.

Author contributions P.B. performed the experiments, simulations and data analysis. W.C. synthesized the sample, performed the experiments and analysed the data. B.H., B.K., M.B., W.W., H.M. and G.G. worked on the theoretical models and simulations of NV contrast under pressure. Z.M.G., V.S., R.J. and X.H. guided the experimental methodologies and sample preparation. S.C., B.I.H., J.E.M., C.R.L. and N.Y.Y. proposed and interpreted the investigations of the sample. Y.L., T.J.S., E.W., Z.W., S.H., S.M., B.C., E.D., Z.M.G. and C.Z. assisted in data collection. C.R.L., T.C., X.H., G.G. and N.Y.Y. supervised the project. P.B., C.R.L. and N.Y.Y. wrote the paper with input from all authors.

Competing interests University of California (co-inventors P.B., B.K., S.H., C.Z., J.E.M., R.J. and N.Y.Y.) filed US Patent Application 63/449,508 titled ‘Multimodal imaging apparatus at ultrahigh pressure’.

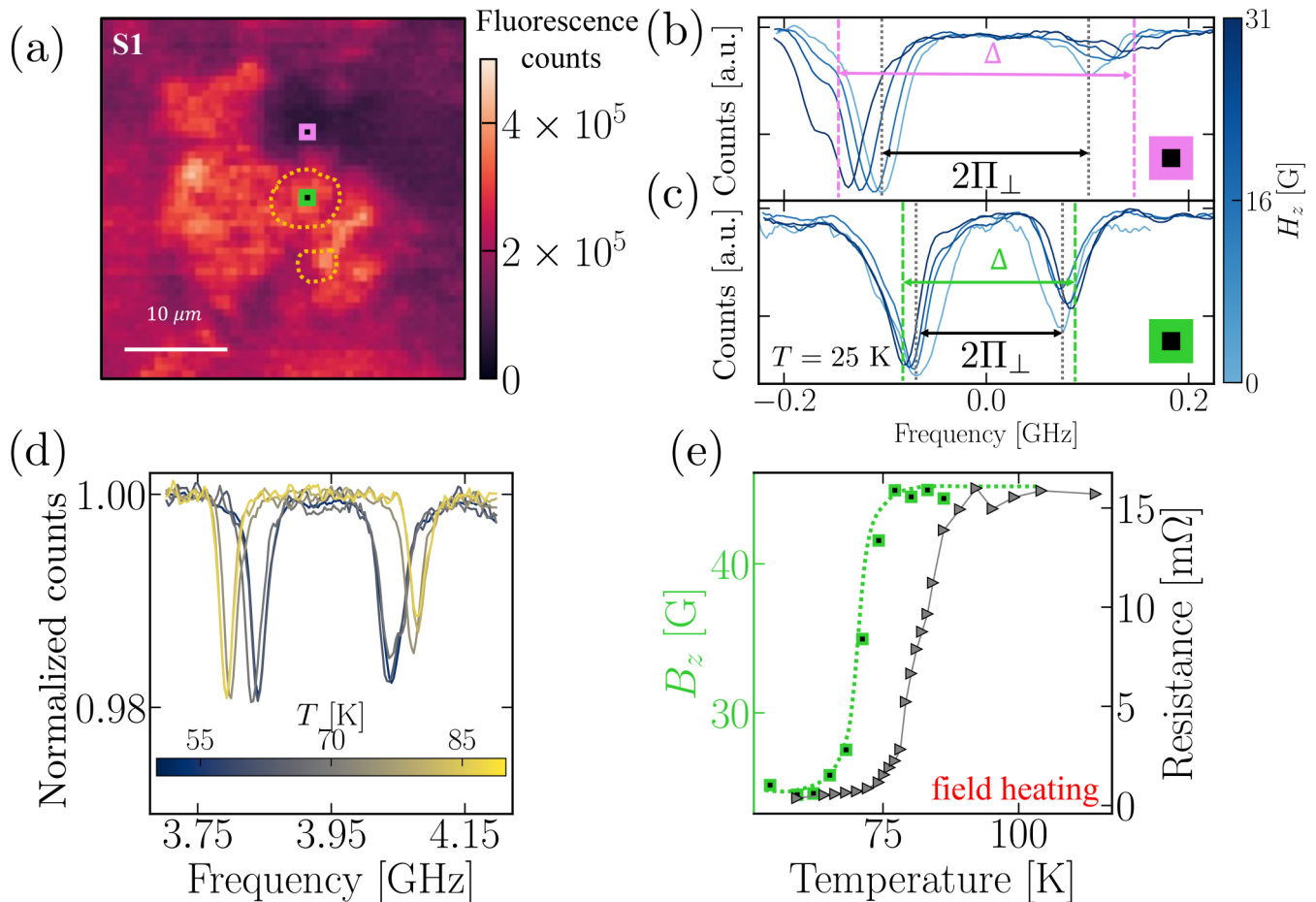
Additional information

Supplementary information The online version contains supplementary material available at <https://doi.org/10.1038/s41586-024-07026-7>.

Correspondence and requests for materials should be addressed to N. Y. Yao.

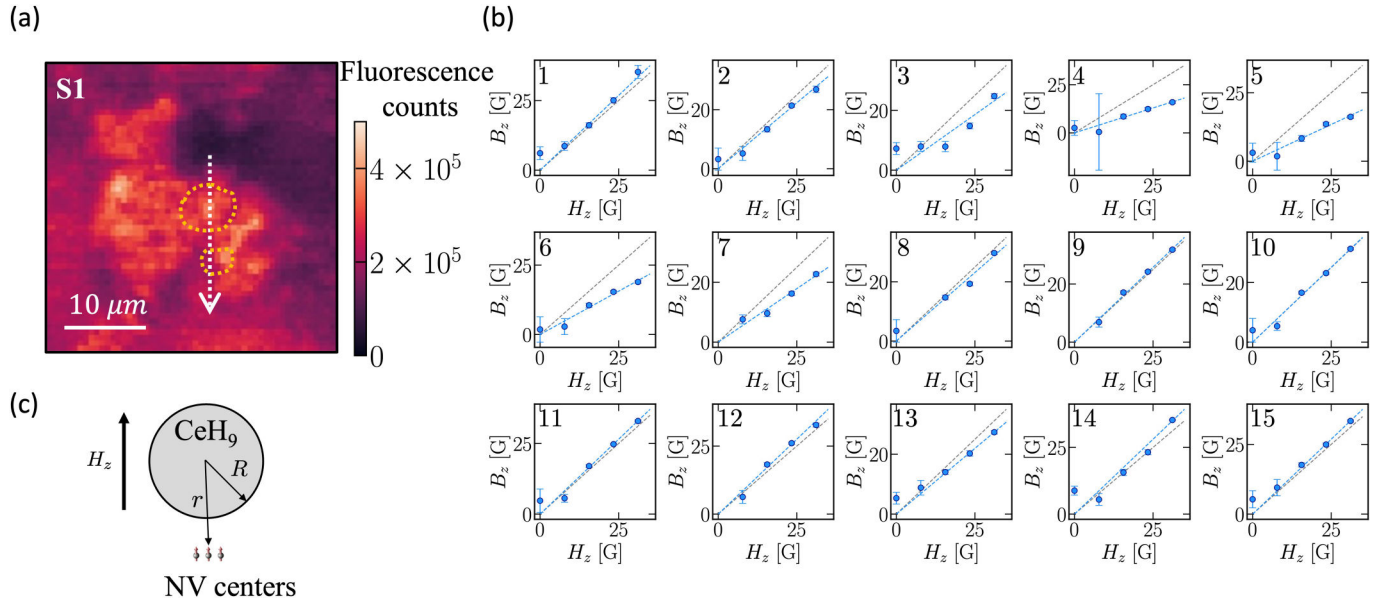
Peer review information *Nature* thanks the anonymous reviewers for their contribution to the peer review of this work. Peer reviewer reports are available.

Reprints and permissions information is available at <http://www.nature.com/reprints>.



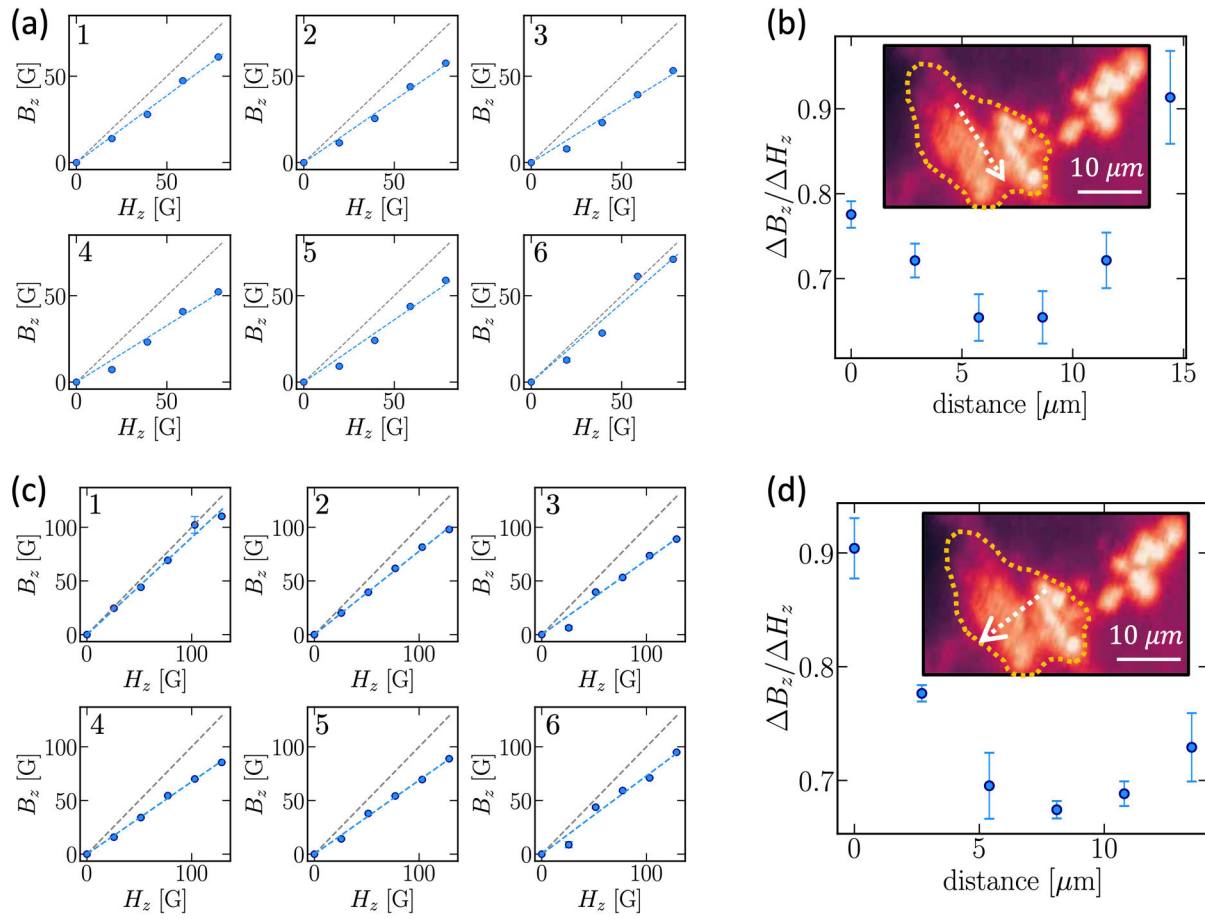
Extended Data Fig. 1 | Studies of diamagnetism in sample S1. **(a)** Confocal fluorescence image of sample S1 showing the identified CeH_3 region (enclosed in dotted yellow line). A comparison of the ODMR spectra measured after zero field cooling to a temperature $T = 25 \text{ K}$ (below T_c) at two spatial locations: one **(b)** away from the CeH_3 region [purple point in (a)], and the other **(c)** on top of the CeH_3 region [green point in (a)]. For clarity, all spectra are centered by subtracting the ODMR shift. As a function of the external field, H_z , the local field, B_z , extracted from these spectra show the diamagnetic response of CeH_3 [main text Fig. 3(f)]. We measure the temperature dependence of this response [at the green point in (a)]. **(d)** Applying $H_z = 47 \text{ G}$ after zero field cooling, we perform ODMR spectroscopy while heating the sample across T_c (field

heating). **(e)** Similar to sample S2 (shown in main text), we observe a clear transition in the diamagnetic response. Four point resistance is measured separately on warming up the sample with $H_z = 0$ (after zero field cooling). For sample S1, we are not able to perform simultaneous magnetometry and electrical resistance measurements due to coupling between the Pt wire for microwave delivery and the transport leads. Although, we expect a suppression in T_c measured via electrical resistance on the application of an external field, the separation between the magnetic and resistive transitions is larger than expected from this effect alone. A reduction of the temperature gradient in the sample on disconnecting the microwave lines may be responsible for this difference.



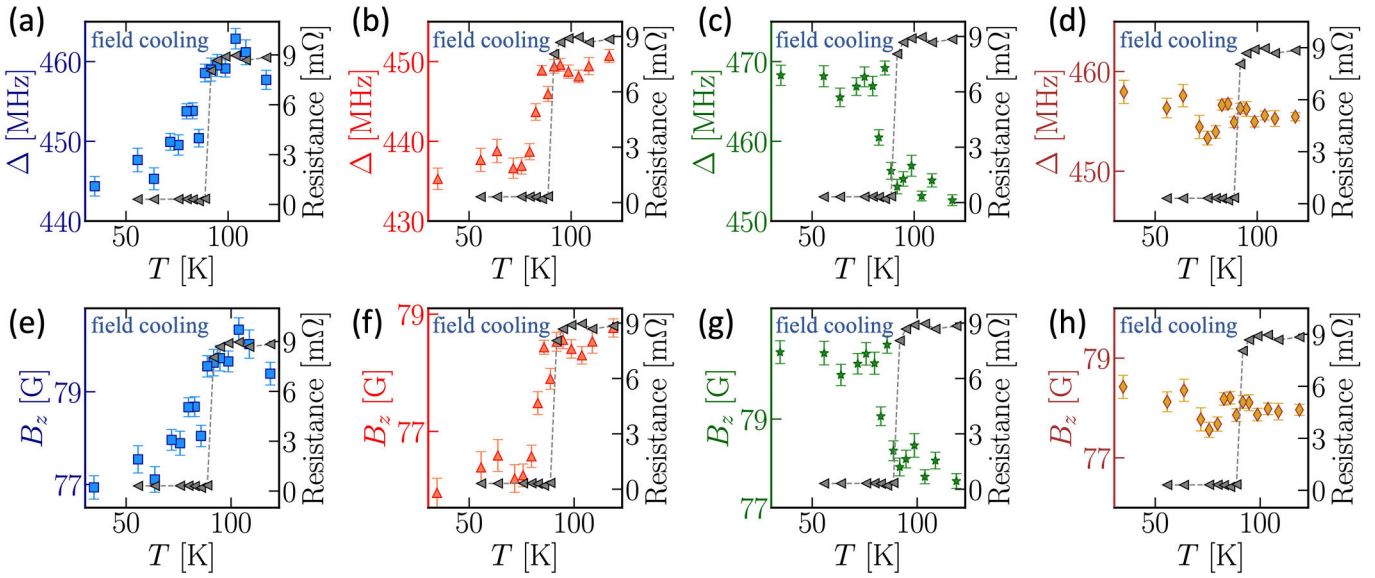
Extended Data Fig. 2 | Spatial studies of diamagnetism in S1. (a) We measure the local suppression in B_z along a line cut shown in the confocal fluorescence scan of sample S1. The slope $s = \Delta B_z / \Delta H_z$ for this study is presented in maintext Fig. 3(g). (b) We show plots of the extracted B_z against the applied external field H_z at fifteen spatial points (indexed) along the line cut. Linear fits to the extracted values of B_z show a clear suppression in two regions of the sample

(enclosed in dotted yellow line in (a)). (c) Schematic geometry we assumed for estimating the CeH₉ sample's diamagnetic properties. We assume a spherical chunk of CeH₉ of radius R with NV centers located at a distance r from the center (directly below the sample). Under the application of an external field H_z along the NV axis, our ODMR measurements yield a suppression factor corresponding to the slope $s = dB_z/dH_z$.



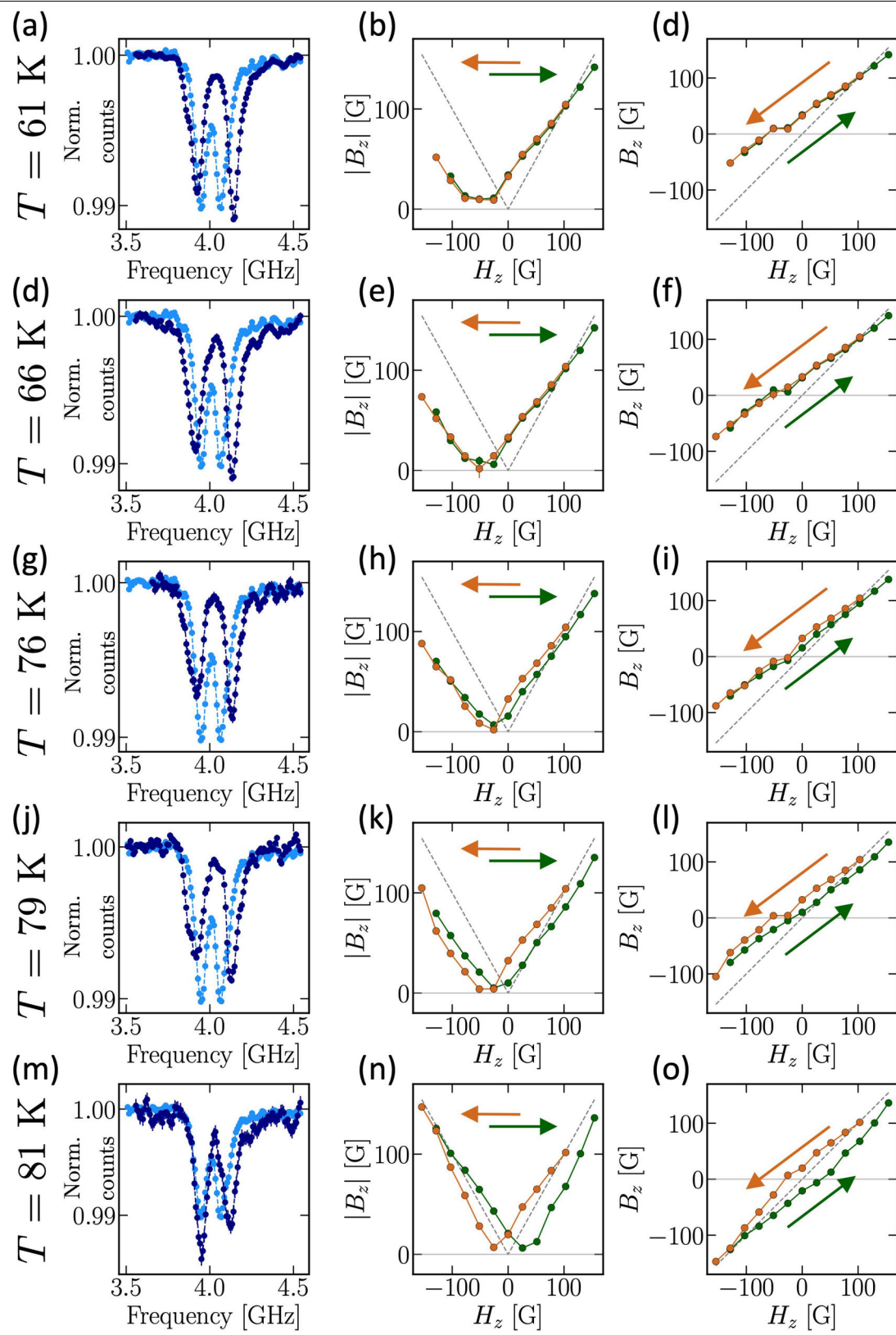
Extended Data Fig. 3 | Spatial studies of diamagnetism in S2. We perform spatial studies of the local suppression in B_z in sample S2 along two orthogonal line cuts. Insets in (b) and (d) show fluorescence scans of S2 with the respective line cuts on top of the identified CeH_9 region (enclosed in dotted yellow line). **(a)** The B_z values extracted from ODMR spectra are plotting against the applied

external field, H_z , for six spatial points (indexed) along the line cut shown in inset of (b). **(b)** Similar to sample S1 [main text Fig. 3(g)], we measure a spatially varying suppression in the local field suggesting the formation of $\approx 10 \mu\text{m}$ regions of CeH_9 via laser heating. **(c-d)** A repeat of the study for six spatial points along an orthogonal line cut (inset of (d)).



Extended Data Fig. 4 | Comparison of ODMR splitting and B_z on field cooling S2 at $H_z = 79$ G. Measurements of four point electrical resistance and the ODMR splitting, Δ , at four spatial locations [shown in maintext Fig. 4(b)]: **(a,b)** two points on top the synthesized CeH₉ (blue and orange), **(c)** one point at the edge of this region (green), and **(d)** one point away from region (yellow). **(a,b)** On top of the CeH₉ region, we measure a decrease in $\Delta \approx (2\pi) \times 15$ MHz as we cool below the transition point. **(c)** In contrast, at the edge of this region, we measure an increase in $\Delta \approx (2\pi) \times 15$ MHz. **(d)** Away from the CeH₉ region we do

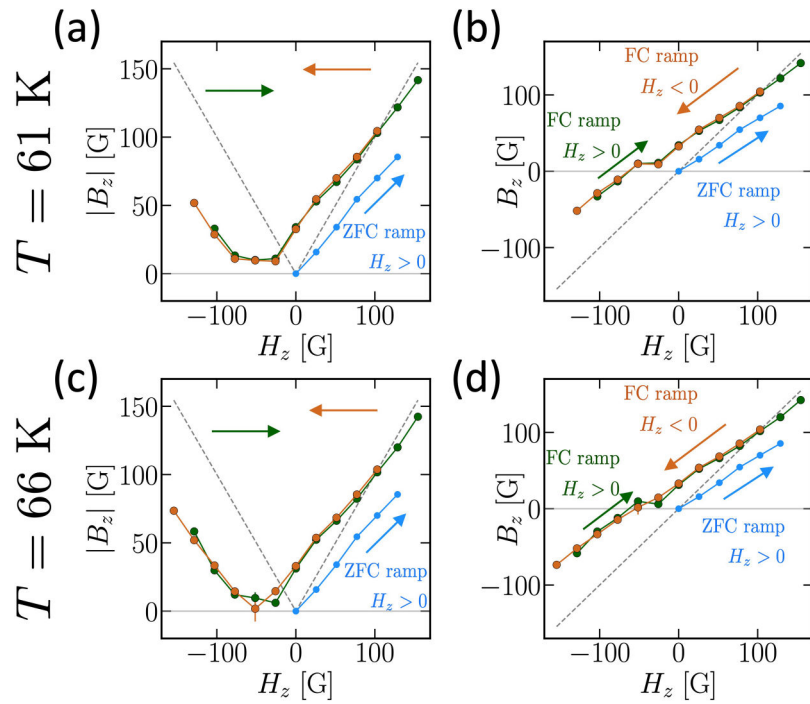
not measure an appreciable change in Δ across the transition point (determined via simultaneous electrical resistance measurements). **(e,f,g,h)** For the Δ values measured at each spatial point, we extract the magnetic field, B_z , based on the $2\Pi_{\perp}$ stress splitting (measured at the same spatial point at $H_z = 0$ G after zero field cooling to $T = 86$ K). Systematic disagreement between B_z and H_z for $T > T_c$ may stem from inaccurate determination of $2\Pi_{\perp}$ or change in the value of $2\Pi_{\perp}$ with temperature.



Extended Data Fig. 5 | Study of flux trapping in sample S2 (full dataset).

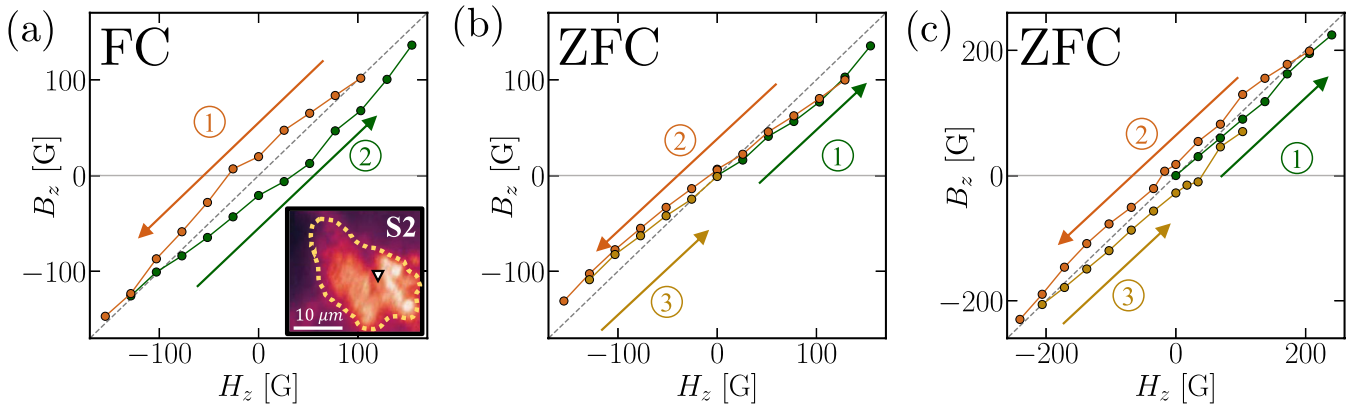
We field cool sample S2 at $H_z = 103$ G to several temperatures (indicated on the left) and ramp the magnitude and direction of H_z [experimental sequence in maintext Fig. 5(f)]. **(a,d,g,j,m)** Dark blue data show the ODMR spectra measured on ramping H_z to zero after field cooling at $H_z = 103$ G to the respective temperatures. Light blue data show the ODMR spectrum measured at $H_z = 0$ on zero field cooling to $T = 81$ K. We observe a markedly higher ODMR splitting in the field cooled data set suggesting the presence of a remnant flux trapped field. The strength of the flux trapped field (i.e., B_z values at $H_z = 0$) decreases with increasing temperature. **(b,e,h,k,n)** We show the measured $|B_z|$ on ramping H_z after field cooling to different temperatures; first, we ramp the external field down from $H_z = 106$ G to $H_z = -154$ G (yellow data points and arrows) and subsequently, we ramp the external field back up $H_z = 154$ G (green

data points and arrows). In order to extract the local $|B_z|$ field from the splitting (Δ), we use the $2\Pi_{\perp}$ splitting measured at $H_z = 0$ on zero field cooling to $T = 81$ K [shown as light blue data in (a,d,g,j,m)]. On switching the direction of the external field ($H_z < 0$), we measure a minimum in $|B_z|$. Since the local field measured at the NV location is the sum of the flux trapped field and H_z , we see an increase in the splitting on further increasing the magnitude of the external field in the negative direction. Based on the continuity of the $|B_z|$ data points across the minimum, we assign a direction (sign) to the local field to extract the local field B_z . **(c,f,i,l,o)** We plot measured local field, B_z , against the applied external field, H_z , at the respective temperatures. We find that a clear increase in hysteresis with increase in temperature. All measurements are performed at the spatial location shown by the inverted white triangle in maintext Fig. 5(c) [also shown in inset in Extended Data Fig. 7(a)].



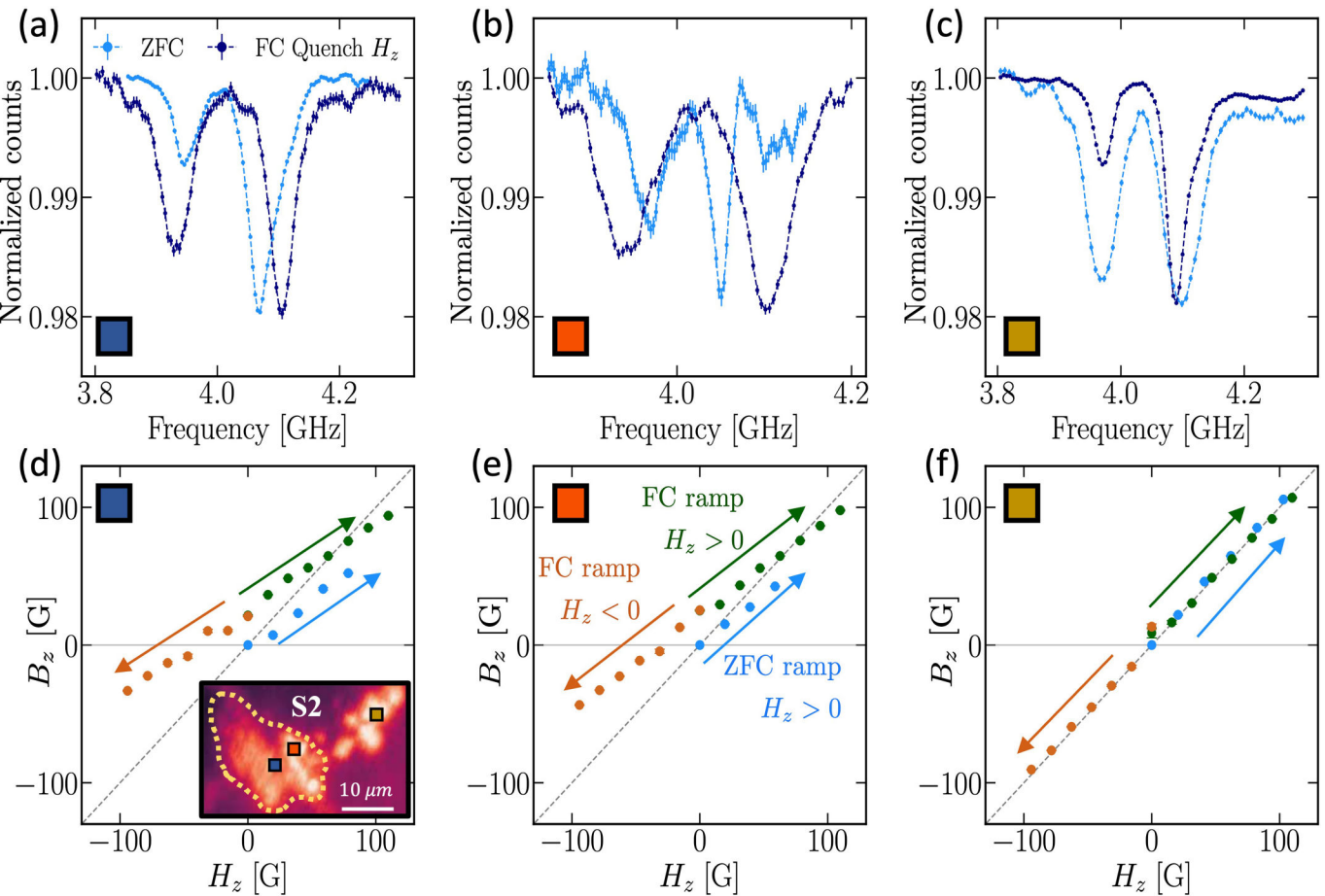
Extended Data Fig. 6 | Comparison of the slopes $s = dB_z/dH_z$ on field cooling and zero field cooling. We reproduce the data for $|B_z|$ vs. H_z measured at **(a)** $T = 61\text{ K}$ and **(d)** $T = 66\text{ K}$ that are also shown in Extended Data Fig. 5(b,e). **(b,c)** Similarly, we show the data for B_z vs. H_z extracted for the respective temperatures. We compare these measurements performed after field cooling and ramping H_z [experimental sequence in maintext Fig. 5(f)] to one

measurement performed after zero field cooling and increasing H_z [light blue data shown in all sub-panels]. We find that, deep in the superconducting phase, B_z exhibits the same slope with respect to H_z on both field cooling and zero field cooling. In the case of field cooling, this suggests that in addition to a trapped flux, there may be a contribution similar to that which gives rise to a local diamagnetic response on zero field cooling.



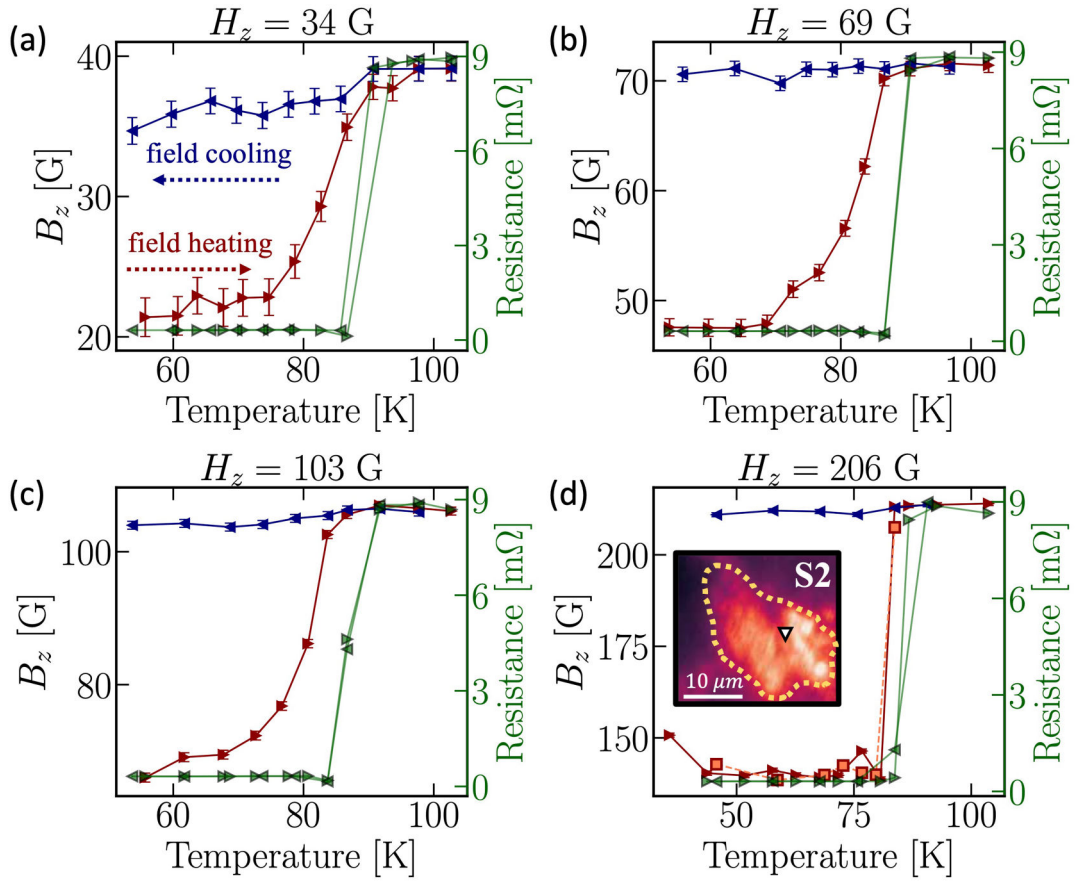
Extended Data Fig. 7 | Flux trapping in S2. We compare the response of the sample on sweeping H_z after field cooling and zero field cooling at $T = 81\text{ K}$. **(a)** On field cooling at $H_z = 103\text{ G}$ we measure a trapped flux. On ramping to large fields in the direction opposite to this trapped flux ($H_z = -154\text{ G}$), we measure an inversion of the flux trapped field. **(b)** In contrast, the sample is robust to flux penetration on zero field cooling. Specifically, on ramping the external field to $|H_z| = 154\text{ G}$ in both the positive and negative directions, we continue to observe a local suppression in B_z without any appreciable flux trapping. **(c)** After zero

field cooling, the sample exhibits flux penetration only on ramping the external field to much larger magnitudes ($|H_z| > 240\text{ G}$). Here, we measure a response similar to the case of field cooling. Specifically, on ramping to a field $H_z = 240\text{ G}$ we find a flux trapped field $B_z = 18\text{ G}$ (measured after returning to $H_z = 0\text{ G}$). Similarly, after ramping to a field $H_z = -240\text{ G}$, the direction of the trapped flux changes (i.e., we measure $B_z = -28\text{ G}$ on returning back to $H_z = 0\text{ G}$). All measurements are performed at the spatial location shown by the inverted white triangle in the fluorescence scan [inset of (a)].



Extended Data Fig. 8 | Spatial studies of flux trapping in S2. We compare the effects of zero field cooling (ZFC) and field cooling (FC) at several spatial points in sample S2 [fluorescence scan in the inset of (d)]: two locations [blue and red points in inset of (d)] on top of the CeH₀ region and one location [yellow point in inset of (d)] away from this region. **(a-c)** We field cool the sample at H_z = 79 G to a temperature T = 36 K and measure the ODMR spectra (dark blue) after quenching the external field to H_z = 0 G. Light blue data show the ODMR spectra measured at the respective spatial locations upon zero field cooling to temperatures (a, b) T = 36 K, and (c) T = 86 K. We see markedly higher splittings on top of the CeH₀ region (a, b) upon field cooling indicating the presence of a flux trapped field. Away from the CeH₀ region (c), we do not observe a significant difference between ZFC and FC data. In particular, Δ for the ZFC spectrum (measured at T = 86 K) is larger by 7 MHz; this difference is likely due to temperature

dependence of the stress splitting, 2Π₁, at this spatial point. **(d-f)** Following the field quench after FC, we determine the local B_z field at the three spatial locations on ramping H_z to positive values (green data points). We make the same measurements on ramping H_z to negative values (orange data points). We also measure B_z as a function of H_z after zero field cooling (blue data points). **(d,e)** On top of the CeH₀ region, our measurements indicate the presence of a flux trapped field upon FC. This contrasts with a local suppression of H_z measured at the same locations upon ZFC. In particular, the slope s = ΔB_z/ΔH_z on field cooling is in quantitative agreement with the slope on zero field cooling. **(f)** Away from CeH₀ region, we see no significant difference in response on ramping H_z after FC and ZFC. To extract B_z at each point, we use the 2Π₁ splitting measured upon zero field cooling at the respective spatial location [light blue spectra in (a-c)].



Extended Data Fig. 9 | Hysteresis on T -sweeps in S2. To study hysteresis on sweeping T , we first zero field cool the sample and apply an external field H_z [main text Fig. 5(d)]. Then, fixing H_z , we heat the sample across the transition (field heating shown in red). Finally, we cool the sample below T_c without changing H_z (field cooling shown in blue). We perform simultaneous electrical resistance (shown in green) and ODMR measurements. Four point resistance measured on field heating (field cooling) are indicated by markers pointing right (left). All measurements are made at the spatial location shown by the

inverted white triangle in fluorescence scan [inset of (d)]. We use the $2\pi_\perp$ stress parameter measured at $H_z = 0$ and $T = 81$ K to extract the local B_z field for all data points. **(a-c)** We observe concurrent transitions in magnetism and electrical resistance. In addition, we see a suppression of T_c with the increase in the magnitude of H_z . **(d)** Surprisingly at high fields ($H_z = 206$ G), we see a clear sharpening of the magnetic transition. To confirm the signal we repeat the measurement on field heating near the transition region (orange squares in (d)).